Experimental investigation into the expansion behaviour of thermally tempered laminated glass plates at asymmetric fracture

Yige Wang[a, b], Xing-er Wang[a, b*], Jian Yang[a, b], Dongdong Xie[a, b], Kai Pang[c], Zhufeng Pan[a, b]

[a] School of Naval Architecture, Ocean and Civil Engineering, Shanghai Jiao Tong University, Shanghai 200240, PR China

[b] Shanghai Key Laboratory for Digital Maintenance of Buildings and Infrastructure, School of Naval Architecture, Ocean and Civil Engineering, Shanghai Jiao Tong University, Shanghai 200240, PR China

[c] School of Engineering, Lancaster University, Lancaster, LA1 4YW, UK

Abstract: The fragments expansion behaviour of thermally tempered glass (TTG) at fracture, can result in the secondary effects that facilitate the fracture or buckling risks of structural glass members. This paper experimentally investigated the fragment morphology and expansion behaviours of thermally tempered laminated glass (LG) plates with different polymeric interlayers and elastic strain energy levels of glass. A computer-vision-based method was adopted for processing stable-state fracture morphology, in order to obtain the fragment density, fracture surface energy and elastic strain energy release at fracture. These parameters were quantitively analysed and compared with those of monolithic glass (MG) plates, identifying the influence of elastic strain energy, intact glass and interlayer. Subsequently, the expansion behaviours were assessed by examining the strain variations on the intact glass and the overall bending deformation. It is found that all specimens exhibit intense strain variations and half sinusoid expansion-induced deformation shapes at asymmetric fracture. Parametric analysis shows that the stiffness disparity between the studied interlayers results in a more than two-fold variation in the maximum in-plane and out-of-plane expansion. In addition, specimens with greater elastic strain energy present higher expansion responses, and the sensitivity of expansion behaviours towards elastic strain energy variations differs across specimens with different configurations. The present study provides insights for further determining the expansion-induced imperfections of structural glass members at post-fracture state.

Keywords: Laminated glass; Thermally tempered glass; Expansion behaviour; Post-fracture state; Elastic strain energy; Fracture morphology

1. Introduction

Thermally tempered laminated glass (LG) has been widely adopted in load-bearing glass structures for its excellent mechanical properties and safety features [1]. Thermally tempered glass (TTG) is produced under a tempering process, in which flat glass is heated up to over 600 °C and then cooled down rapidly using the jets of air. A parabolic residual stress distribution along the thickness with compression on the surface and tension in the mid-plane can then be generated [2, 3]. Parameters such as glass temperature before cooling and the heat transfer coefficient during cooling significantly control the magnitude of residual stress [4, 5]. According to the magnitude of surface compressive stress, TTG can be further divided into heat-strengthened glass and fully tempered glass [6]. The surface compressive stress gives the glass higher resistance to breakage, since the small surface flaws will not grow until the surface compressive stress is exceeded by the external load [7]. In addition, TTG will be fractured into small blunt fragments in the case of failure, which can ensure a higher degree of safety compared with the sharp shards of float glass [8]. These small fragments stem from the release of stored elastic strain energy in TTG, and the size of fragments is highly dependent on the residual energy state, as suggested in the existing literature [8-12].

However, recent studies show that the post-fracture load-bearing capacity of TTG may be weaker than that of annealed glass. Zhao et al. [13] tested the out-of-plane post-fracture performance of LG plates having various thermal treatment levels. The results indicate that plates with larger fragments provide better resistance. A similar conclusion is drawn from the through-cracked tensile test and random-cracked tensile test with different fracture patterns conducted by Chen et al. [14]. Another drawback of TTG, which is also the primary concern in this paper, is the trend of volume expansion due to the release of stored elastic strain energy at fracture. It can generate initial imperfections in glass members that may introduce detrimental second-order effects. After fragmentation, the stored elastic strain energy $U_{E,\ stored}$ will convert into energy for creating new fracture surfaces $U_{surface}$ and kinetic energy $U_{kinetic}$ [11, 15, 16]:

$$U_{E,\ stored}+U_{loading}=U_{E,\ remaining}+U_{surface}+U_{kinetic}+U_{other} \quad (1)$$

where $U_{loading}$ is the energy of external loading, $U_{E,\ remaining}$ is the remaining elastic strain energy and U_{other} is the energy consumed by other effects such as sound and heat. Nielsen et al. [16] presented a numerical model to evaluate a single fragment's stress redistribution and deformation during this process. The investigation shows that the fragment tends to expand at the edges and shrink at the centre. In addition, it is also found that the stress redistribution and deformation are highly related to the magnitude of the residual surface compressive stress and the geometric parameters of the fragment. Subsequent studies, as reported in [17], further validated this numerical method by comparing the surface profiles before and after the fracture.

For a monolithic TTG plate or beam, the fragment expansion would only show in-plane free expansion in all directions. However, in the case of LG, which consists of glass layers bonded by polymeric interlayers, fragment expansion can induce unfavourable deformation and stress under certain circumstances. Initially, the introduction of interlayers aims at utilising the strong adhesion between the glass and interlayer. This adhesion not only enables glass fragments to be retained on the interlayer after fracture, thereby reducing the risk of glass-related injuries [18], but also makes it possible for stress redistribution after partial breakage, allowing for substantial resistance to member failure [19]. Regarding fragment expansion, the bonding by interlayer could transform the free expansion of a single fractured glass layer into a comprehensive expansion of the entire member. As shown in Fig. 1, when the initial self-equilibrium state fails, the fragments tend to push each other, leading to a macro expansion of the whole fractured glass layer. If the interlayer and glass are well bonded, the expansion of the fractured glass layer would be transferred to the neighbouring glass layers by the interlayer. Furthermore, the whole member would show a trend of out-of-plane deformation, when the fracture mode is asymmetric. The interlayer plays an important role in this process. Additionally, it should also be noted that commonly adopted interlayers, like polyvinyl butyral (PVB), ionomer (SentryGlas®, SG), ethylene-vinyl acetate (EVA) and thermoplastic polyurethane (PU), all have high nonlinearity as well as time and temperature dependency [20-23]. These features make it complex to accurately predict LG members' expansion behaviour during the post-fracture state.

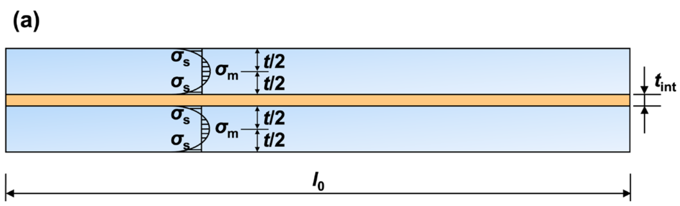

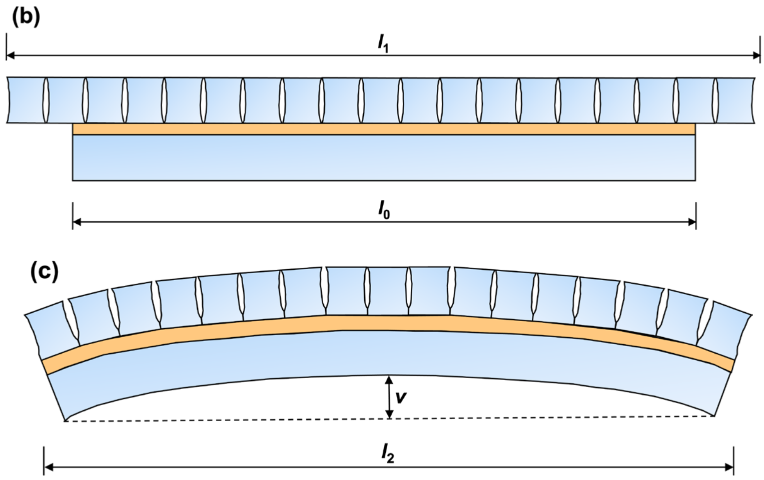

Fig. 1 Fractured thermally tempered LG (fracture mode: asymmetric): (a) initial state; (b) expansion without considering the effect of interlayer; (c) Expansion considering the effect of interlayer

To date, the investigations on the expansion behaviour of TTG at the member level are still limited. Experimental data published in this field are scarcely available, and there is no general analytical model for estimating both in-plane and out-of-plane expansion. Weis et al. [24] investigated the effect of interlayer types on the fracture morphology of two-layer LG plates. In this study, noticeable out-of-plane expansion were found when LG plates were asymmetrically fractured. Wang et al. [25] observed volume expansion and fragments movement induced strain variations, after cracking certain layers of the multi-layered LG panels. It is also found that the fragments expansion and tension-stiffening effect [26, 27] can contribute to the out-of-plane stiffness of specific partially cracked LG panels. However, neither of these studies have recorded the detailed expansion-induced deformation and strain values. In the investigation of the in-plane post-fracture performance of three-layered LG beams with different interlayers, the expansion of TTG was measured [28]. The strains recorded on the intact glass layer showed rapid changes after fracture. After that, they decayed gradually and then reached a plateau. This might be related to the time-dependent property of interlayer, claimed by the researchers. Similar to the study by Weis et al. [24], the out-of-plane expansion only happened when the fracture mode was asymmetric, and a lateral sag of 30-32 mm was observed in the case that the central and one of the outmost glass layers failed. In addition, an equivalent non-isotropic temperature gradient was introduced on the fractured glass layer to numerically simulate the expansion effect. Based on the flexibility method, the temperature gradient can be determined by the collected mid-span strain value during the post-fracture stage. Subsequently, Biolzi et al. [29] examined the out-of-plane resistance of LG plates with different interlayers, and the out-of-plane expansion was measured during the experimental process. A similar equivalent method as [28] was conducted to simulate the expansion of LG plates, and the numerical results were in good agreement with the experimental results. Nevertheless, the application of this method is highly experiment-dependent, which restrains its general engineering use. To this end, a refined analytical attempt was carried out by Nielsen et al. [30], which combined the aforementioned numerical method [16] and the statistical findings on TTG fracture morphology by Pourmoghaddam et al. [8, 15]. The proposed equivalent temperature differences (ETD) model provides an effective method of estimating the average in-plane expansion of TTG. However, the primary defects of this method are that it overlooks the interlayer bonding effect and the bending behaviour under the asymmetric fracture mode. Additionally, the author pointed out that the application of the proposed model also depended on the accurate determination of the stiffness for the fractured thermally tempered glass. Based on the equivalent temperature differences (ETD) model [30], Wang et al. [31] proposed an equivalent expansion model for multi-layered LG beam. This model can provide conservative predictions to the out-of-plane deformation of LG beam with different geometries, surface compressive stress and effective modulus of fractured glass layers. In the newly published specification CEN/TS 19100-3 [32], the expansion during the post-fracture stage is emphasised that the unfavourable effects should be considered in the post-fracture buckling design. An empirical formula is provided in this specification to estimate the out-of-plane expansion, but it is exclusively applicable to PVB LG members. Members with different interlayer types and glass surface compressive stress are beyond the scope of this empirical formula.

Thus, this paper aims to improve current understandings of post-fracture behaviours of thermally tempered LG members, with a special concern on expansion-induced imperfections which can facilitate the engineering glass design when introducing the stiffness and integrity of fractured glass members. The novelty of this research lies in the facts that:

(1) A comprehensive experimental study was devised and conducted, for the first time, to investigate the secondary effects (i.e., fragments expansion-induced strain variations and overall bending deformation) in thermally tempered LG plates at asymmetric fracture.

(2) The influences of interlayer type and elastic strain energy on fragment morphology and

expansion behaviours were identified. These findings can provide designers with more targeted approaches to address the expansion-induced imperfections.

In this study, 48 thermally tempered LG plates, with different interlayer types (SG and PVB), glass thicknesses (6 mm, 8 mm and 12 mm) and surface compressive stress (60-105 MPa), were cracked into an asymmetric fracture mode. The post-fracture responses of these LG plates were characterised by their fracture morphology and expansion behaviours. In the former part, the geometric features of fragments were extracted through a computer-vision-based method for a quantitative analysis of fracture morphology and the elastic strain energy release after fracture. Then, the expansion behaviours in terms of expansion-induced strain variations on the intact glass and overall bending deformation were presented and compared. It is followed by a parametric analysis to investigate the effects of key variables, such as interlayer type and elastic strain energy levels, on expansion behaviours.

2. Experiment

2.1 Specimen design

LG plates with a total of 16 configurations were tested. There were three replicates for each configuration. The specimens were laminated with two TTG layers and one interlayer with a size of 600 mm × 300 mm. The fabrication and measurement of specimens were conducted in two steps: 1) glass sheets fabrication and surface compressive stress measurement, 2) glass lamination and overall thickness measurement.

In the first step, glass sheets with different thickness and surface compressive stress were fabricated to achieve different elastic strain energy levels. Three thicknesses, i.e., 6, 8 and 12 mm, were utilised. Additionally, the tempering conditions were carefully controlled to achieve three surface compressive stress levels, denoted by a, b and c, which covered a surface compressive stress ranging from 60 MPa to 105 MPa. Surface stress metre (type JF-1E) was used to obtain the surface compressive stress of each glass sheet. Measurements were carried out according to GB 15763.2 [33], and the surface compressive stress of each glass sheet was averaged by the measurements at four specific points, as illustrated in Fig. 2. For each specimen, the surface compressive stress across different measurement points showed great uniformity with the highest coefficient of variation of 2.61 %.

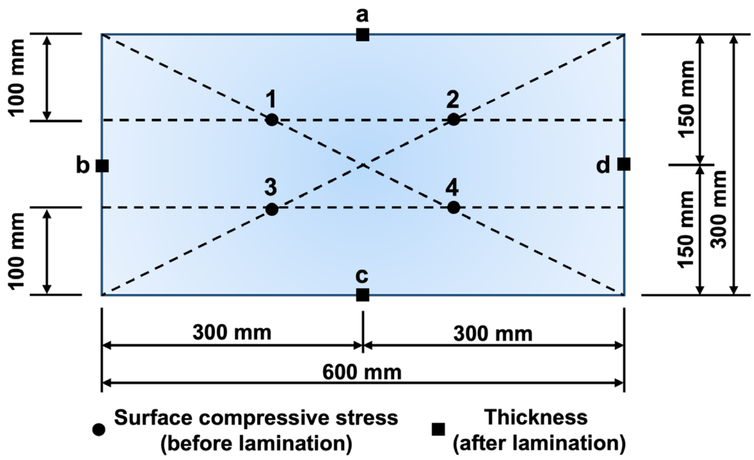

Fig. 2 Surface compressive stress and thickness measurements

In the second step, two glass sheets with the same thickness and surface compressive stress, along with one interlayer, were laminated. The present study used two types of interlayer materials, PVB and SG, both with a thickness of 1.52 mm. The PVB interlayers adopted were Trosifol® UltraClear B200 NR, and SG interlayers were SentryGlas Xtra® SGR6000, both supplied by Kuraray China Co., Ltd. The shear relaxation modulus at 30 °C for both interlayers is shown in Table 1. The true total thickness of each specimen was measured at each edge’s midpoint with a Vernier calliper, as illustrated in Fig. 2. The measurements of each specimen across different points also showed great uniformity, as the observed highest coefficient of variation was only 1.42 %.

Table 1 Shear relaxation modulus $G(t)$ (unit: MPa) at 30 °C [34]

Interlayer	Load duration							
	3 sec	30 sec	1 min	5 min	10 min	1 hour	1 day	5 days
SG	101	84.8	80.1	55.1	38.2	26.0	8.97	7.13
PVB	0.69	0.50	0.47	0.41	0.35	0.33	0.19	0.12

The detailed information for each series, including the mean value and the standard deviation (Std) of measurements across different specimens within each series, is listed in Table 2. The specimens were supplied by Henan Zhongbo Glass Co., Ltd. (Manufacturer A) and Shanghai Shenbo Glass Co., Ltd. (Manufacturer B). LP08c-SG series and LP12c-SG series were provided by Manufacturer B due to the production line adjustments of Manufacturer A. Although the LP08c-SG series shows limited differences in average surface compressive stress compared with LP08b-SG series, it is also included to provide further insights for future refined numerical and analytical studies. Prior to testing, all plates were visually inspected for defects, and none were noted.

Table 2 Configurations of tested LG plates

Series	Surface compressive stress level	Surface compressive stress σ_s (MPa)		True total thickness t_{tot} (mm)		Interlayer Type	Manufacturer
		Mean	Std	Mean	Std		
LP06a-SG	Low	76.82	1.89	13.63	0.11	SG	A
LP06b-SG	Mid	91.50	1.17	13.38	0.13	SG	A
LP06c-SG	High	103.41	2.12	13.44	0.04	SG	A
LP08a-SG	Low	69.53	1.03	17.46	0.11	SG	A
LP08b-SG	Mid	84.56	1.47	17.41	0.07	SG	A
LP08c-SG	High	86.55	0.58	17.31	0.06	SG	B
LP12a-SG	Low	60.80	1.08	25.40	0.07	SG	A
LP12b-SG	Mid	71.09	1.33	25.43	0.07	SG	A
LP12c-SG	High	85.23	0.18	25.25	0.09	SG	B
LP06a-PVB	Low	76.82	1.89	13.35	0.07	PVB	A
LP06b-PVB	Mid	91.50	1.17	13.30	0.07	PVB	A
LP06c-PVB	High	103.41	2.12	13.39	0.13	PVB	A
LP08b-PVB	Mid	84.56	1.47	17.42	0.11	PVB	A
LP08c-PVB	High	103.70	1.42	17.47	0.21	PVB	A
LP12a-PVB	Low	60.80	1.08	25.54	0.08	PVB	A
LP12c-PVB	High	94.20	2.49	25.51	0.05	PVB	A

2.2 Experimental setup

This experiment intended to crack one glass layer of the specimen, which would generate an asymmetric fracture mode. Then, as shown in Fig. 3, the central deformation along the *x*-axis and strain variations at six designated locations (*x*-direction: 11, 12, 13 and *y*-direction: 21, 22, 23) on the intact glass layer were collected to evaluate the out-of-plane and in-plane expansion of the specimen, respectively. Since the expansion was symmetric about the *y*-axis under the current cracking load [28], only six strain gauges were installed on the glass surface. Three strain gauges were installed along the midspan of the *x*-direction (data denoted by ε_{11}, ε_{12}, ε_{13}), and the rest were along the *y*-direction (data denoted by ε_{21}, ε_{22}, ε_{23}).

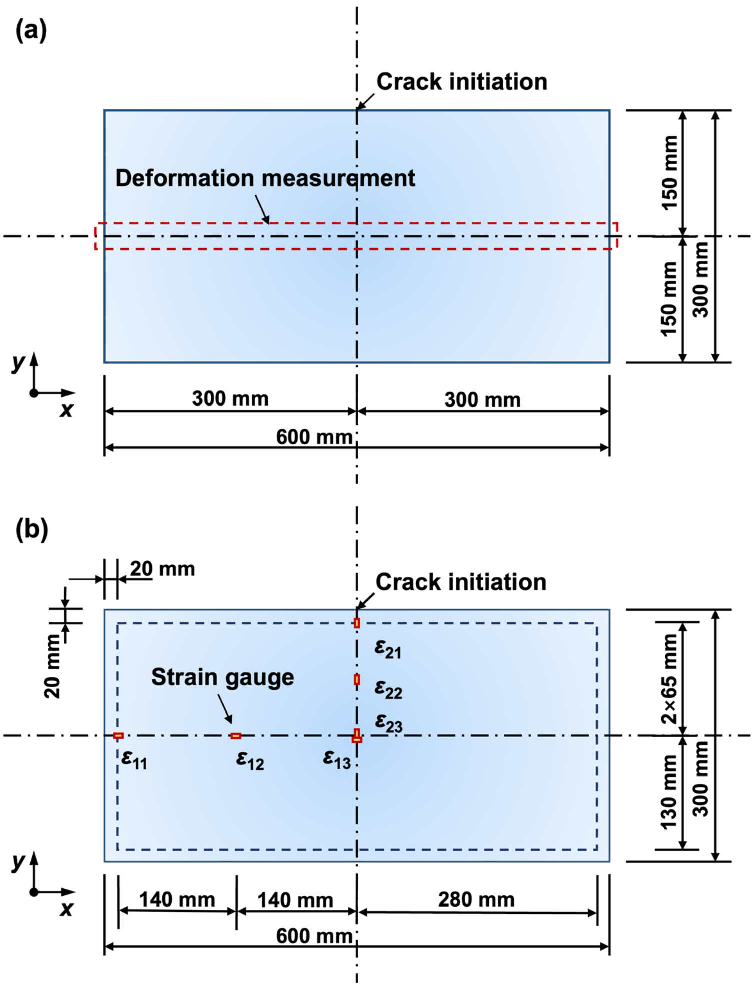

Fig. 3 Expansion responses measurement: (a) deformation measurement; (b) strain variation measurement

The experiments were carried out at temperature of 29 ± 2 °C. An expansion evaluation system was set up to record the in-plane and out-of-plane expansion responses. As shown in Fig. 4, the specimen was placed vertically to diminish the influence of gravity. Four corner bolts were used to fix the specimen and acrylic panel together, with the aim of reducing the constraints imposed by the boundary conditions, while limiting the specimen's movement as much as possible during the fragment expansion. Flexible pads were also employed with bolts to provide an additional softer constraint on specimens. Furthermore, after collecting the expansion responses of each specimen, a thin polycarbonate plate can be easily placed between the acrylic panel and the specimen. The combined optical properties can enhance the projection of fracture morphology, which has been successfully employed in a previous study [12]. To ensure the strain gauges on the intact glass layer can be connected to the data acquisition system, the acrylic panel was designed with openings at both the x-axis and y-axis. In previous studies, LVDT (Linear Variable Differential Transformer) [35] and laser devices [36] were the two main sensors to measure the initial imperfection of glass members. These sensors usually have an accuracy of 0.01 mm which can sufficiently meet the requirements to capture initial deformation. However, in most preliminary tests, the limited specimen size has resulted in relatively small out-of-plane deformation. To this end, the chromatic confocal scanner, which can provide data with a high accuracy of 0.025 μm, was used in this study to enhance the reliability of results. The chromatic confocal scanner utilises the wavelength dependence of longitudinal chromatic aberration and analyses the spectral components reflected by light to achieve its functionality [37, 38]. As a non-contact measuring sensor, it can significantly reduce the interference to the specimen during the post-fracture state. Although this device can conduct measurements on transparent materials, the result could be discrete in the present study as the measurement area was on the fractured glass layer. Thus, non-transparent tapes were adhered to this area to obtain continuous results. Since the adhesion area was limited and the stiffness of the tape was much lower than that of the interlayer, the influence of tape can be neglected. The chromatic confocal scanner was mounted on a motorised wagon, which could slide on an aluminium guiding rail parallel to the specimen at a low and constant speed.

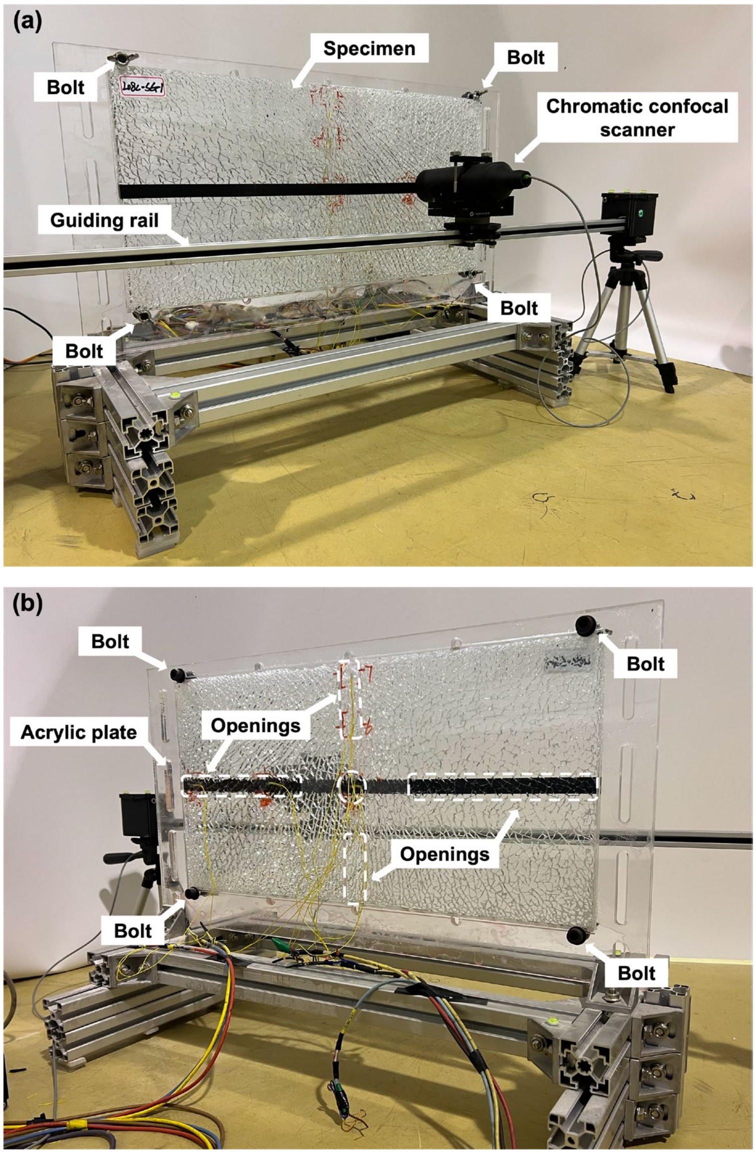

Fig. 4 Expansion measurement system: (a) front view (fractured glass layer); (b) back view (intact glass layer)

The specimens were fractured according to EN 12150-1 [39] with the crack initiation shown in Fig. 3. In the present study, a hammer with a tungsten steel tip was used to fracture the specimen. The hammer was qualitatively performed to ensure U_{loading} in Eq. (1) remained basically consistent. This can be supported by the minor variations in fracture surface energy and expansion responses observed among specimens within the same series in the following section. As illustrated by Eq. (1), when the fracture surface energy and expansion responses are relatively uniform, it can be inferred that the energy introduced by external loading is similar for glasses with the same elastic strain energy.

3. Results and discussion

3.1 Fracture morphology

The specimens were cracked in an asymmetric fracture mode as described in Section 2, and the MV-SUA2000C-T industrial camera (with a resolution of 5488 × 3672) was used to collect the fracture morphology. It should be mentioned that the fracture morphology was collected after obtaining the expansion results and the crack generation became stable (with no further occurrence of secondary cracking). Fig. 5, Fig. 6 and Fig. 7 show the typical fracture morphology of each series following distortion correction and removal of extraneous information. Since the release of stored elastic strain energy in the fractured glass layer drives both the fracture morphology and the expansion behaviours of the LG plates, the elastic strain energy per surface area U_0 [15, 16] for the fractured glass layer is used to represent the total amount of stored elastic strain energy $U_{\mathrm{E,\ stored}}$ by the residual stress and it can be calculated by Eq. (2):

$$U_0=\frac{1}{5}\frac{(1\text{-}v)}{E}t\sigma_{\mathrm{s}}^2 \tag{2}$$

where the Young's modulus E and Poisson ratio v of the TTG are 70 GPa and 0.23, respectively. [30] The thickness t refers to the nominal thickness of the fractured glass layer, and σ_{s} is the average surface compressive stress of the fractured glass layer.

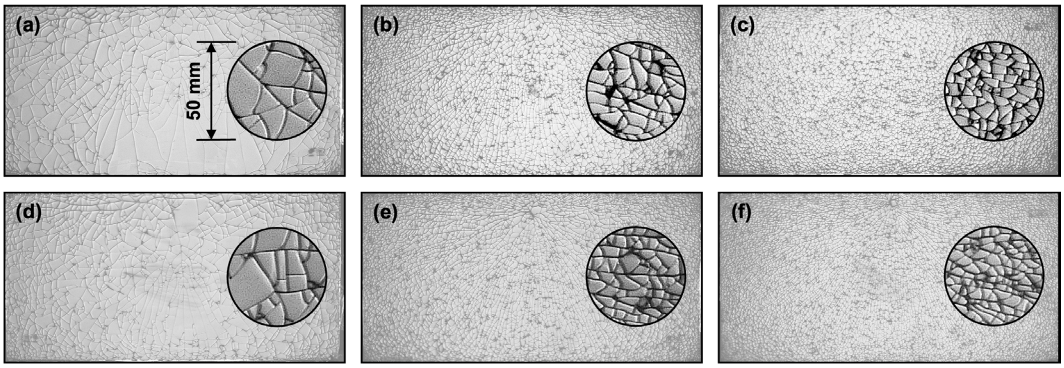

Fig. 5 Fracture morphology of the LP06 series: (a) LP06a-SG-1 (U_0=77.9 J/m^2); (b) LP06b-SG-1 (U_0=110.5 J/m^2); (c) LP06c-SG-3 (U_0=141.2 J/m^2); (d) LP06a-PVB-1 (U_0=77.9 J/m^2); (e) LP06b-PVB-1 (U_0=110.5 J/m^2); (f) LP06c-PVB-1 (U_0=141.2 J/m^2)

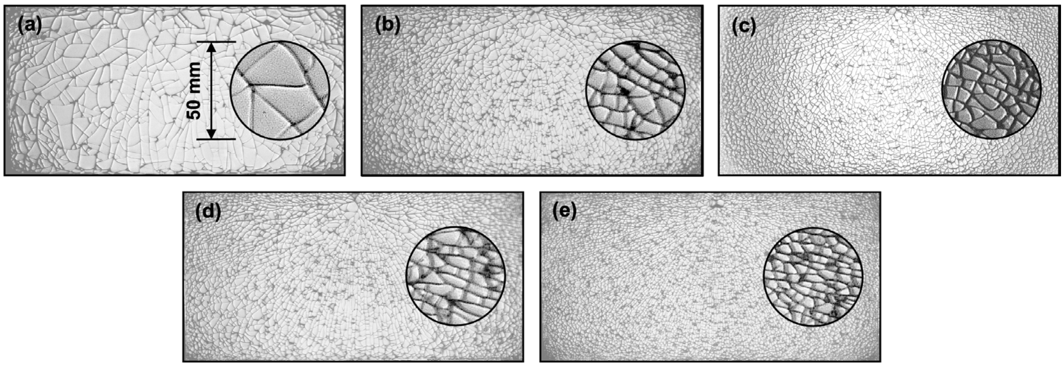

Fig. 6 Fracture morphology of the LP08 series: (a) LP08a-SG-2 (U_0=85.1 J/m^2); (b) LP08b-SG-2 (U_0=125.8 J/m^2); (c) LP08c-SG-2 (U_0=131.8 J/m^2); (d) LP08b-PVB-1 (U_0=125.8 J/m^2); (e) LP08c-PVB-3 (U_0=189.3 J/m^2)

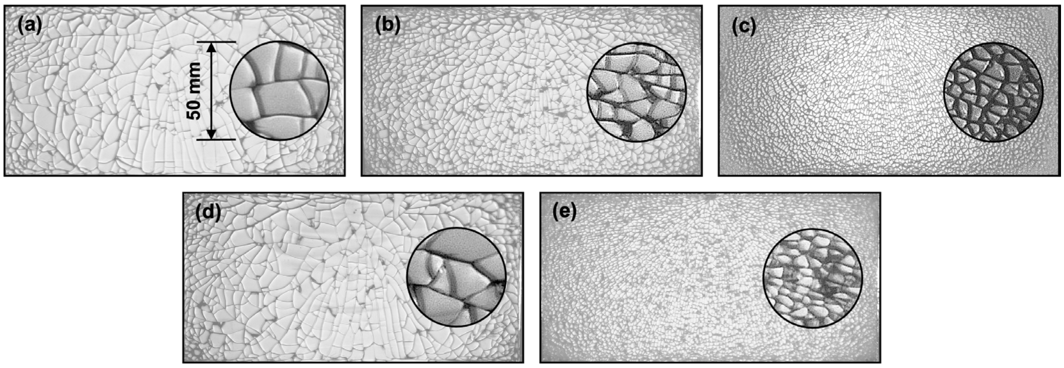

Fig. 7 Fracture morphology of the LP12 series: (a) LP12a-SG-3 (U_0=97.6 J/m^2); (b) LP12b-SG-1 (U_0=133.4 J/m^2); (c) LP12c-SG-3 (U_0=191.8 J/m^2); (d) LP12a-PVB-1 (U_0=97.6 J/m^2); (e) LP12c-PVB-3 (U_0=234.3 J/m^2)

To quantify the fragment feature, a computer-vision-based method was employed with the open-source image processing software Fiji [40]. Fig. 8 illustrates the image processing procedures of the local image of LP06c-SG-2 with a size of 50 mm × 50 mm. After pre-processing (distortion correction and cropping), pixel-based segmentation of images was produced with the plugin Trainable Weka Segmentation [41], where each image was classified into crack branching and fragments. The segmentation outputs were then further optimized and processed into skeletonized images. Quantification of fragment features was performed by morphological segmentation of individual fragments using the MorphoLibJ plugin [42]. This allowed for the determination of fragment numbers and perimeter, which were then utilized for fragment feature analysis. Key fracture morphology parameters were obtained based on the analysis results, as summarized in Table A1 and Table A2.

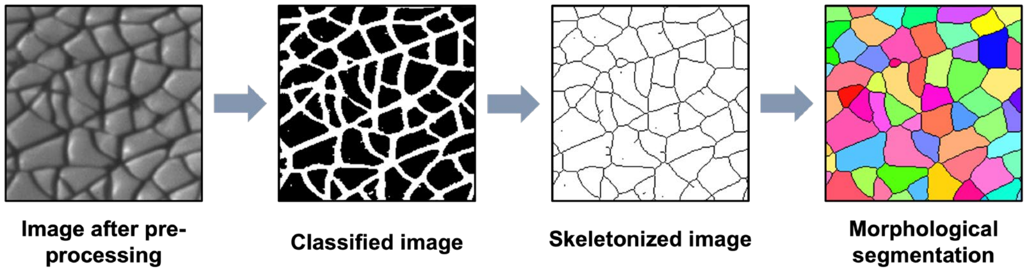

Fig. 8 Procedure of fracture morphology image processing (local image of LP06c-SG-2)

3.1.1 Fragment density

This research aims to explore the post-fracture behaviours of LG plates from a global scale, so the fragment density λ_G was studied by dividing the fragment number by the whole plate area. The assessment of a global fragment density can also facilitate the development of a refined numerical model based on feature points-based fracture morphology reconstruction [12, 43-45]. Fig. 9 shows the average results of each case, along with the data from a previous study [12]. In Ref [12], a comprehensive investigation was conducted on the morphological characteristics of monolithic glass (MG) plates of dimensions 600 mm × 300 mm, which were identical to the LG plates in the present study.

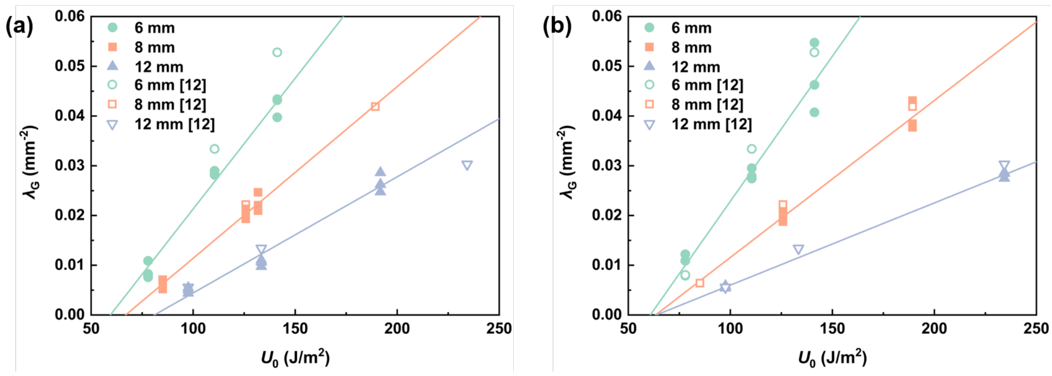

Fig. 9 The relationship between fragment density λ_G and elastic strain energy per surface area U_0: (a) SG series; (b) PVB series

With a given interlayer type and glass layer thickness, specimens having the higher elastic strain energy have a higher fragment density, indicating more elastic strain energy is transformed into energy for generating new fracture surfaces. In addition, linear regression was used to fit present data points. Strong linear relationship can be observed in all SG series and 6 mm PVB series.

Although the data for 8 mm and 12 mm PVB series were limited to only two elastic strain energy groups, the linear relationship may still be inferred and they were connected by lines to facilitate further analysis. It is also noticed that the introduction of an intact glass layer and interlayer, compared with monolithic cases in [12], has an impact on the fragment density. At a relatively low elastic strain energy, the fragment density for LG plates and MG plates, with similar elastic strain energy, exhibits minimal difference. However, as the elastic strain energy increases to a higher level, the density differences become more significant. Most MG plate data is higher than that of LG plate. As the tested LG plate is fractured in an asymmetric mode, the fracture surface growth is affected by the intact glass layer and interlayer. The release of stored elastic strain energy, which contributes to fracture surface generation, can be restrained. Thus, it is rational to observe a lower fragment density in LG plates.

Moreover, from Fig. 5 to Fig. 7, the fragments also show significant morphological disparities. Specimens with higher elastic strain energy have small fragments with blunt shapes. Besides, butterfly-shaped fragments are commonly observed at the crack initiation in these specimens, from which the cracks propagate and branch (e.g., LP08c-PVB-3 in Fig. 10(a)). The cracks can be further divided into primary cracks and secondary cracks. The secondary cracks are in the orthogonal direction of the primary cracks, and they are usually driven by the residual stress field [46]. As a result, the secondary cracks arise after the main cracks, which can also be observed in the expansion responses and will be explained in the following section.

For specimens with low strain energy, the crack propagation and branching are much milder, resulting in larger fragments. In addition, their fragments are more irregular and sharper, which can be further divided into two categories in the present study. As shown in Fig. 10(b), strip-shaped fragments with a large aspect ratio can be observed in the lower-middle part of the impact influence zone [47]. Apart from these areas, most of the fragments are chunk-shaped with becoming smaller when being closer to the edge. This differs from the higher strain energy cases where all fragments are basically with the similar size and shape.

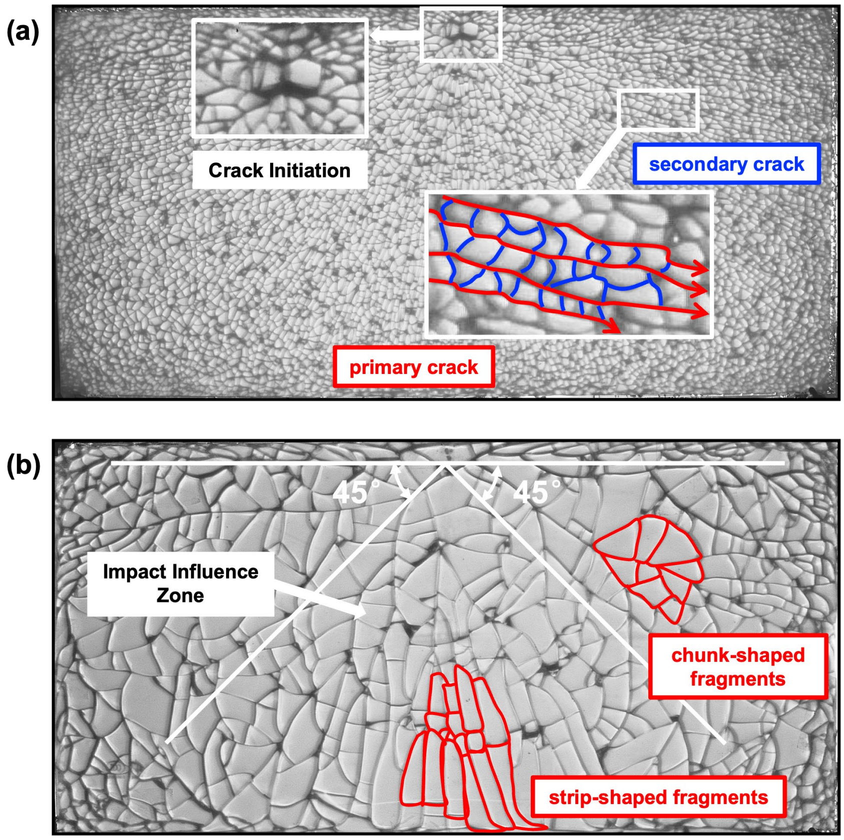

Fig. 10 Comparison of two typical fracture morphology: (a) LP08c-PVB-3 (U_0=189.3 J/m^2); (b) LP12a-SG-3 (U_0=97.6 J/m^2)

3.1.2 Fracture surface energy

According to [12], the total amount of a specimen's fracture surface energy U_{surface} can be calculated by Eq. (3):

$$U_{\text{surface}}=2\gamma_0 \cdot L_{\text{C}}t=2\gamma_0 \cdot \varphi \tag{3}$$

where L_{C} is the total crack length and it can be estimated by the data of the fragments' perimeter. Although the fracture surface energy can be affected by elastic modulus difference due to glass composition and testing temperature [48, 49], it was not the main concern to determine the value of fracture surface energy here. In addition, except for LP08c-SG series and LP12c-SG series, all other glass specimens as well as those from the previous study [12], were made of the same raw material and were supplied by the same manufacturer. In this regard, γ_0 can be considered as a constant and the value of fracture surface energy only depends on $L_{\text{C}}t$, which was defined as the coefficient φ.

The energy transferring of cracks generation was estimated by dividing the elastic strain energy per surface area U_0 by the fracture surface energy U_{surface}:

$$\frac{U_{\mathrm{surface}}}{U_0} = \frac{10\gamma_0 E}{1\text{-}\nu}\cdot\frac{L_{\mathrm{C}}}{\sigma_{\mathrm{s}}^2} = \frac{10\gamma_0 E}{1\text{-}\nu}\cdot\psi \tag{4}$$

It was also noticed that the parameters γ_0, E and ν would remain constant for specimens made of the same raw material. Thus, coefficient ψ, which can be estimated by $L_{\mathrm{C}}/\sigma_{\mathrm{s}}^2$, was defined to assess the energy transferring rate from elastic strain energy to fracture surface energy.

The two defined energy coefficients φ and ψ for present LG plates are calculated and presented in Fig. 11 and Fig. 12, along with the results of MG plates from [12], to characterize the fracture surface energy and energy transfer across the whole plates. All the presented specimens were provided by manufacturer A.

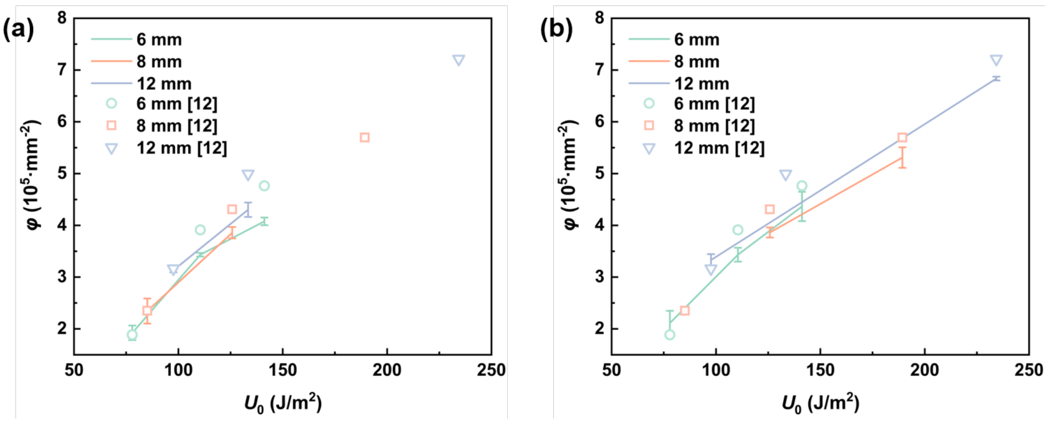

Fig. 11 Coefficient φ of present LG plates and MG plates from [12]: (a) SG series; (b) PVB series

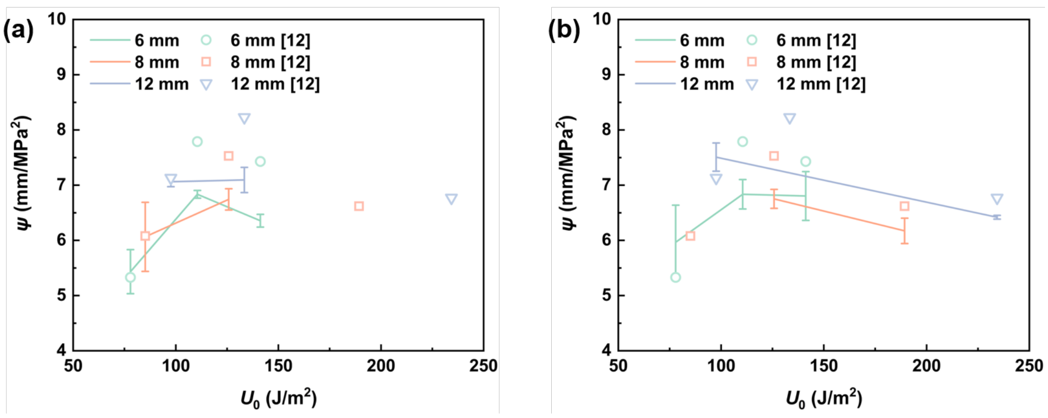

Fig. 12 Coefficient ψ of present LG plates and MG plates from [12]: (a) SG series; (b) PVB series

As shown in Fig. 12, it can be observed that for MG plates with the same thickness [12], coefficient ψ initially increases and then decreases with the increments in elastic strain energy. There is a certain threshold during this process, after which a higher proportion of elastic strain energy is released or secondarily stored in other forms, such as fragment expansion, rather than fracture surface energy. The variation trend of coefficient ψ remains the same for the 6 mm LG plates. For the 8 mm and 12 mm LG plates, only two elastic strain energy groups are available for comparison in each interlayer series. However, for each case, the relative magnitudes of coefficient ψ between the two elastic strain energy groups are consistent with the MG plates [12], except the 8 mm SG series. Taking the 8 mm PVB series in Fig. 12(b) as an example, when the elastic strain energy U_0 increases from 125.8 J/m^2 to 189.3 J/m^2, MG plates' coefficient ψ presents a decrease in from 7.53 mm/MPa^2 to 6.62 mm/MPa^2. A similar decrease can also be observed for the LG plates, with the average coefficient ψ dropping from 6.75 mm/MPa^2 to 6.12 mm/MPa^2. It should be noted that the energy transferring rate from elastic strain energy to fracture surface energy is not consistent with the value of fracture surface energy. As shown in Fig. 11, as the elastic strain energy increases, the fracture surface energy, represented by coefficient φ, continuously rises. Specifically, for the 6 mm SG series, as the elastic strain energy U_0 increases from 110.5 J/m^2 to 141.2 J/m^2, the average coefficient ψ experiences a decline of 0.37 mm/MPa^2 (Fig. 12(a)), while the average coefficient φ increases from $3.913\times10^5\cdot$mm^{-2} to $4.765\times10^5\cdot$mm^{-2} (Fig. 11(a)). The increased fracture surface energy can also be evidenced by the increased fragment density as presented in Fig. 9. Meanwhile, a higher value of coefficient ψ does not imply lower fragment expansion behaviour. Once the elastic strain energy of a glass specimen is improved, its expansion behaviour will increase as well, which is illustrated in Section 3.4.2.

Compared with the MG cases from [12], the crack generation of present asymmetrically fractured LG plates is constrained by both intact glass layer and interlayer. The constraints of the intact glass layer present different effects at various elastic strain energy levels. At the same thickness, for the cases with relatively higher elastic strain energy, both coefficient φ and ψ of the LG plates are observed to be lower than those of the corresponding MG plates, such as the last two elastic strain energy groups of 6 mm PVB and SG series. This indicates that not only the value of fracture surface energy but also the transferring rate decreases due to the constraint of the intact glass layer. However, for the case of low elastic strain energy level, certain LG plates show higher values on both coefficient φ and ψ than the MG plates, e.g., the first elastic strain energy group of

6 mm and 12 mm PVB series. This variation is assumed to be affected by the differences in crack initiation positions between the present study and the previous study [12]. In Ref [12], MG plates were fractured at three different positions, i.e., corner point, midpoint of the long edge and midpoint of the centre. The data presented in Fig. 11 and Fig. 12 from [12] are average values of the three crack initiation positions. The previous study [12] suggests that the majority of the obtained fragment perimeter data points fall into a favourable distribution range for each tempering level. As shown in Fig. 5, Fig. 6 and Fig. 7, the fragments of specimens with mid or high surface compressive stress level are uniformly distributed with rather similar shape and size. Therefore, most of these fragments are within this distribution range. It is also noted that within this range there is no significant difference in the probability density of fragment perimeter with different crack initiations [12]. Consequently, the effect of crack initiation on total crack length L_C could be limited, resulting in similar values on coefficient φ and ψ for cases with different crack initiations. However, for specimens with low surface compressive stress level, the favourable distribution range may be more referred to the rather small and regular fragments around the boundary. There are a greater number of these fragments than the central irregular fragments, thus making the boundary fragments fall within the favourable distribution range. However, the central irregular fragments, which are not within this range, may be more decisive on total crack length L_C, as these fragments have higher perimeters than the boundary fragments. The irregular chunk-shaped fragments are observed with significant differences due to the variations of crack initiation in [12]. Cases with corner point and midpoint of the centre crack initiations might have a lower total crack length L_C in Eq. (3) and (4). It should also be noted that, for cases with different crack initiation positions, the crack propagation is constrained differently from the boundary, which could contribute to variations in fracture surface energy and energy transfer. It is presumed that specimens with a low elastic strain energy level are more prone to be affected by the boundary at fracture.

Differences in the values of coefficient φ and ψ are also observed when comparing SG LG plates with PVB LG plates, as shown in Fig. 11 and Fig. 12. It is assumed that the differences are affected by the disparity in interlayer stiffness. At most temperatures, SG shows a significantly stiffer property than PVB [50, 51], which can offer higher constraints on crack generation. Thus, SG LG plates have lower values of coefficient φ and ψ than corresponding PVB LG plates. However, as the constraining difference between the two interlayers is significantly lower than intact glass, the observed coefficient differences between SG LG plates and PVB LG plates are lower than those between LG plates and MG plates in most cases.

3.2 In-plane expansion

The strain gauges recorded the strain variations on the intact glass layer, and the typical curves for each series are shown from Fig. 13 to Fig. 15. To illustrate strain variations more clearly, the time point of fracture initiation is set as the time-axis origin and a 12-minute interval is presented.

It can be seen that the strains of both PVB and SG series will instantly reach a significant value after fragmentation. For the PVB series, a peak can be observed after the hammer impact for most measuring points. The strains decline rapidly at first, and then the decaying gradually slows down until reaching a relatively constant strain value. It is also observed that the strains ε_{13} of LP06c-PVB-3 (Fig. 13 (f)) and LP06b-PVB-3 (Fig. 13 (e)), ε_{11} of LP12a-PVB-3 (Fig. 15 (d)) still follow a minor declining trend until the end of the recorded period. By contrast, most strains in SG series will enter the plateau stage as soon as the fracture without noticeable decaying, except for the marginal values ε_{11} and ε_{21}. This difference can be ascribed to the different mechanical properties of the PVB and SG interlayers. Standard PVB usually shows relatively soft, ductile and viscoelastic properties. SG is a much 'stiffer' material and can offer better adhesion to glass [51-53]. Because of this, the constraint of PVB to fragments expansion would decline with time, which indicates that the in-plane expansion would gradually turn into in-plane deformation of the fractured glass layer. Thus, strain responses collected on the intact glass layer would decline gradually with time. As for the SG series, SG can constrain the expansion immediately after fracture and transfer this effect to the intact glass layer, thus a strain decaying is less likely to happen. Such a high decaying rate is not consistent across all positions, a similar pattern to the PVB series can be observed in the marginal strains ε_{11} and ε_{21} in the SG series. This is due to the relatively weaker constraints provided by SG and the intact glass layer when closer to the edge. Nevertheless, this is insignificant in the PVB series, since the constraint effect of PVB itself is weak. It should be mentioned that the variations in strain are more pronounced in the initial 4 to 5 minutes, with the magnitudes staying relatively constant thereafter.

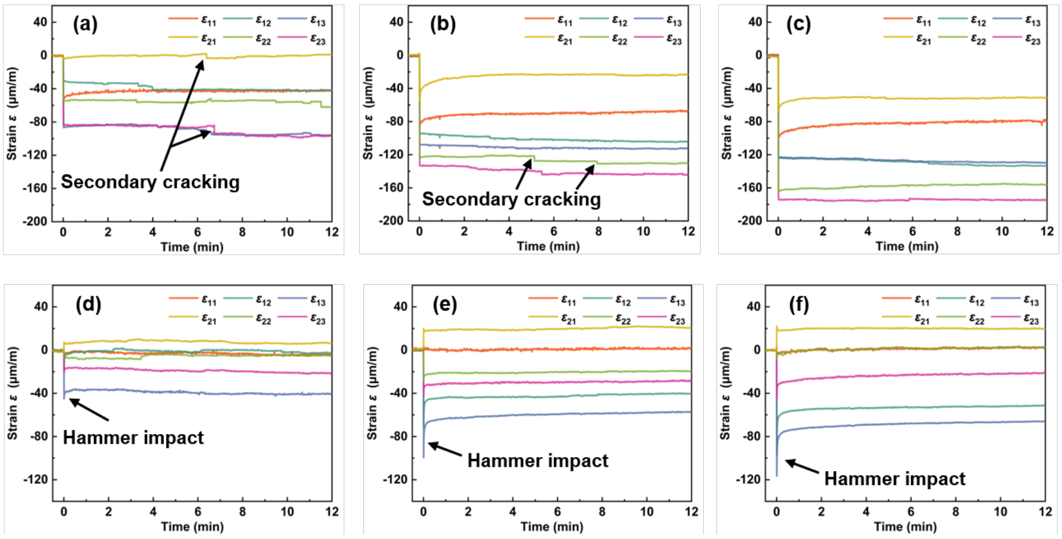

Fig. 13 Typical in-plane expansion results of the LP06 series: (a) LP06a-SG-3; (b) LP06b-SG-2; (c) LP06c-SG-2; (d) LP06a-PVB-2; (e) LP06b-PVB-3; (f) LP06c-PVB-3

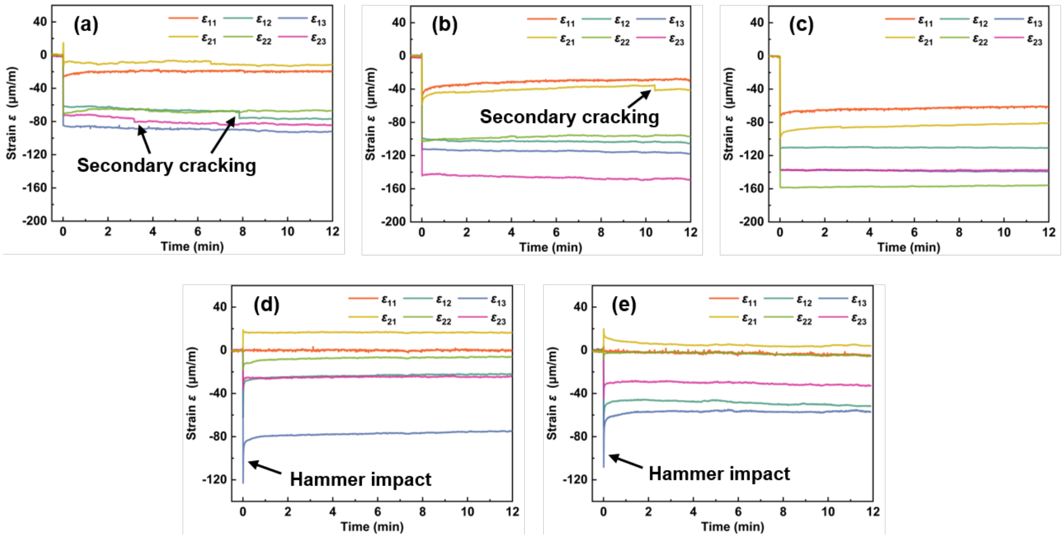

Fig. 14 Typical in-plane expansion results of the LP08 series: (a) LP08a-SG-1; (b) LP08b-SG-2; (c) LP08c-SG-1; (d) LP08b-PVB-3; (e) LP08c-PVB-3

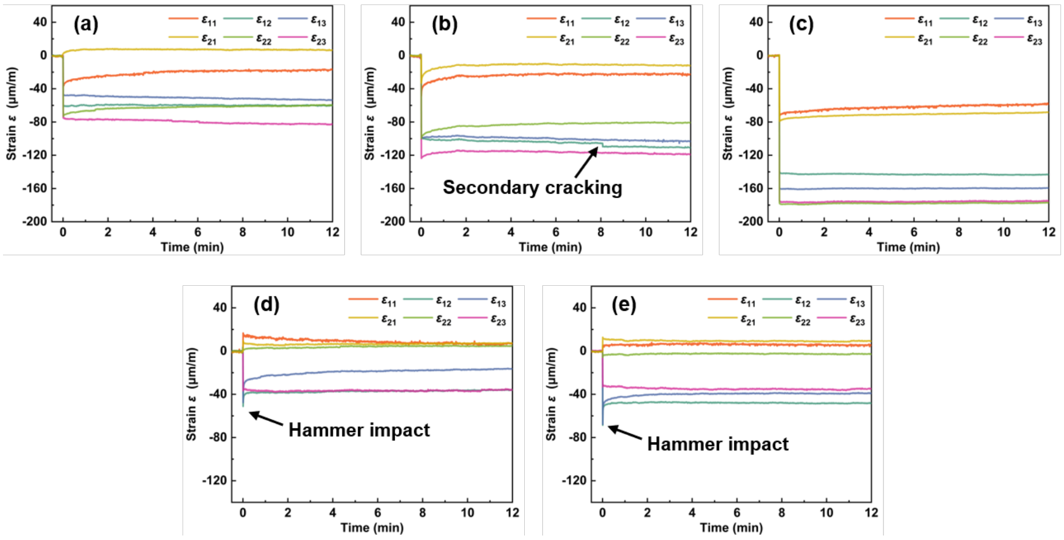

Fig. 15 Typical in-plane expansion results of the LP12 series: (a) LP12a-SG-1; (b) LP12b-SG-3; (c) LP12c-SG-2; (d) LP12a-PVB-3; (e) LP12c-PVB-1

Another interesting phenomenon observed in the in-plane expansion curves is the sudden change of strain values during the stable state. This variation is more evident for the SG LG plates with low and mid surface compressive stress levels, whilst the high surface compressive stress level series do not present evident fluctuation. As shown in Fig. 13(a), the recorded values of ε_{21} and ε_{23} have sudden drops at 7 min and then remain nearly constant. Similar changes can also be observed in ε_{12} and ε_{23} in Fig. 14(a), ε_{21} and ε_{22} in Fig. 14(b), as well as ε_{12} in Fig. 15(b). In the case of ε_{22} in Fig. 13(b), the strains present drops more than once. By contrast, the curves of the high surface compressive stress level series (e.g., Fig. 13(c), Fig. 14(c) and Fig. 15(c)) are smooth without any sudden drops. As for the PVB series, none of the specimens is observed with apparent strain drops, with the exception of LP06a-PVB-2 in Fig. 13(d).

A probable reason for this fluctuation might be attributed to the expansion-induced secondary crack branching after fragmentation. As explained before, the secondary cracks, mainly driven by the release of strain energy, are generated later than the primary cracks [46, 54]. In addition to this delaying feature, the generation of secondary cracks is also time-dependent. The studies conducted by Takahashi [55] and Aratani et al. [56] show that the occurrence of secondary cracks will continuously increase in the first 100 s after fragmentation initiation. The time-dependent characteristic of secondary crack growth was also recorded in [24] by calculating the fragment density within 15 mins after fragmentation. In tested specimens, the expansion-induced by secondary cracks is transferred to the intact glass layer, generating a sudden drop in strain value with a feature of decaying and time dependence. Moreover, as explained before, this observation is also dependent on the interlayer mechanical property. As a stiffer material, SG can transfer this expansion effectively, while PVB is more likely to absorb this effect. Overall, as can be seen from Fig. 13 to Fig. 15, the effect of secondary crack on the strain magnitude is limited compared with that of primary cracks. As most strain values become nearly constant 5 mins after fragmentation, the 5-min state is defined as the stable expansion state of specimens in the following investigation.

3.3 Out-of-plane expansion

The out-of-plane expansion-induced deformation of LG plates can be determined by the recorded position state by the chromatic confocal scanner. The initial imperfection of the tested plates after installation to the acrylic panel was measured before performing the fragmentation. This initial imperfection Δ_1 commonly includes the initial geometrical imperfection of LG plate Δ_{glass}, misalignment from the installation of LG plate $\Delta_{install}$ and geometrical imperfection of the guiding rail Δ_{rail}:

$$\Delta_1=\Delta_{glass}+\Delta_{install}+\Delta_{rail} \tag{5}$$

The second position state was measured 5 mins after fragmentation, and denoted by Δ_2 (Eq. (6)). It is obvious that Δ_{glass}, $\Delta_{install}$ and Δ_{rail} will remain the same, while the expansion-induced deformation Δ_0 and fracture disturbance $\Delta_{fracture}$ are introduced in Δ_2. Since the specimens are restrained by bolts on the four corners and the fracture process is instantaneous with a relatively minor disturbance, the fracture disturbance is not taken into account:

$$\Delta_2=\Delta_{glass}+\Delta_{install}+\Delta_{rail}+\Delta_0 \tag{6}$$

As a result, the out-of-plane expansion Δ_0 can be determined by the recorded Δ_1 and Δ_2. This can avoid the discussion on geometrical imperfections of the guiding rail, which can be determined by the mirror measurement method [35].

The out-of-plane expansion-induced deformation shows high consistency within each series. A typical curve of each series is selected for comparison as shown in Fig. 16, Fig. 17 and Fig. 18. It can be seen that the out-of-plane results coincide with the framework of small deformation, and the results vary with interlayer, glass thickness and surface compressive stress. Among all the results, the minimum out-of-plane expansion-induced deformation is 0.22 mm, from LP12a-PVB-1 as shown in Fig. 18(b). In contrast, the maximum value, 2.62 mm in LP06c-SG-1 (Fig. 16(a)), is more than ten times the minimum value. It should be noticed that all out-of-plane results are with half sinusoid shapes, which are more regular than the initial imperfection of glass members [35]. Besides, the maximum out-of-plane expansion-induced deformation of each specimen, denoted by $\Delta_{0,\,\max}$, consistently situates at the specimen centre. The results also suggest that once a LG member is fractured into the asymmetric mode, without appropriate boundary restraints the member might show a half-sinusoid expansion-induced shape similar to its first eigenmode. This can significantly increase the buckling risk of LG members during the post-fracture state.

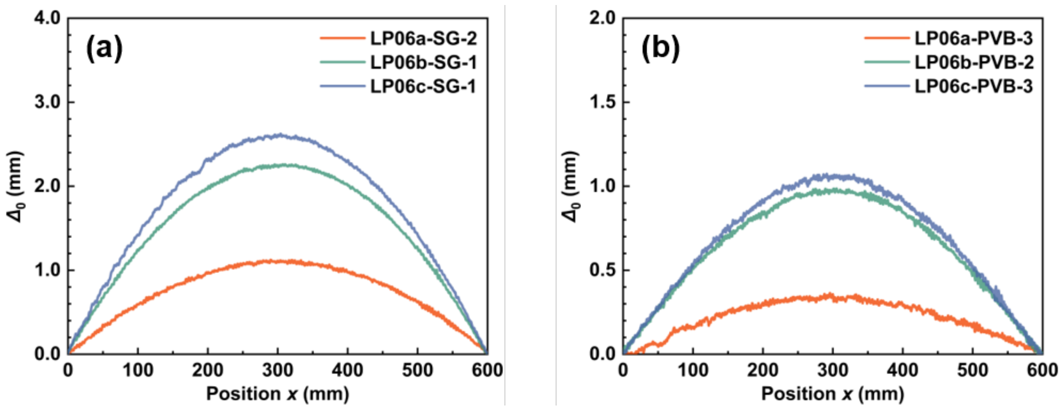

Fig. 16 Typical out-of-plane expansion results of the LP06 series: (a) SG LG plates; (b) PVB LG plates

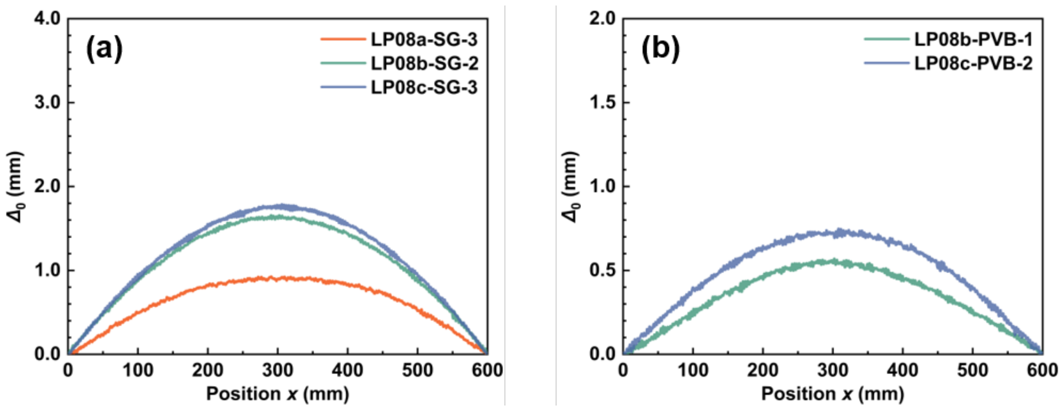

Fig. 17 Typical out-of-plane expansion results of the LP08 series: (a) SG LG plates; (b) PVB LG plates

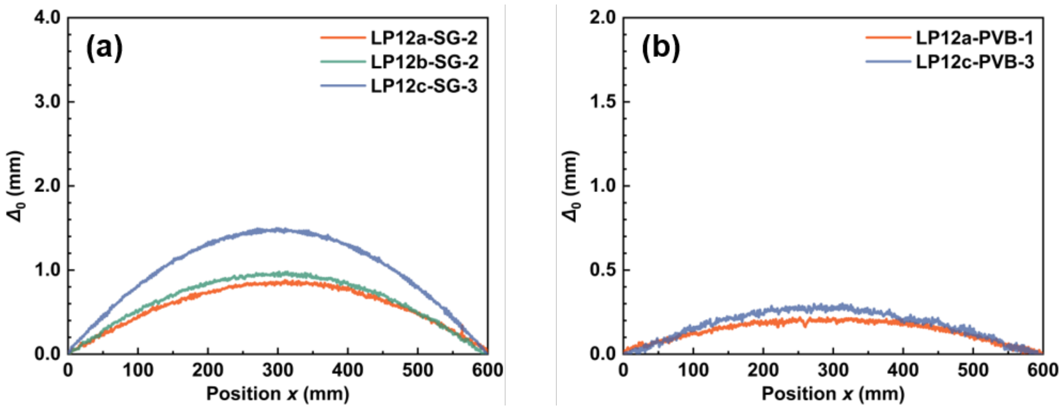

Fig. 18 Typical out-of-plane expansion results of the LP12 series: (a) SG LG plates; (b) PVB LG plates

3.4 Parametric analysis

As described in Section 3.2, most LG plates' strains remain stable 5 mins after fragmentation. Thus, the in-plane and out-of-plane results at 5 mins are used to identify the expansion behaviour of LG plates with various factors, i.e., interlayer type and elastic strain energy. However, marginal strains ε_{11} and ε_{21} are neglected due to the interference by the strong reflection of stress waves at the boundaries, which leads to highly intense and irregular secondary cracks [57]. The collected marginal strain data varies with a wide magnitude interval and shows limited uniformity in most cases, which is unfavourable to seeking insights. For this reason, only strain values ε_{12}, ε_{13}, ε_{22} and ε_{23} and maximum out-of-plane expansion-induced deformation $\Delta_{0,\ \mathrm{max}}$ at 5 mins are selected to analyse the associated influence on the in-plane and out-of-plane expansion of LG plates. The typical expansion responses of LP06, LP08 and LP12 series are shown in Fig. 19, Fig. 20 and Fig. 21, respectively.

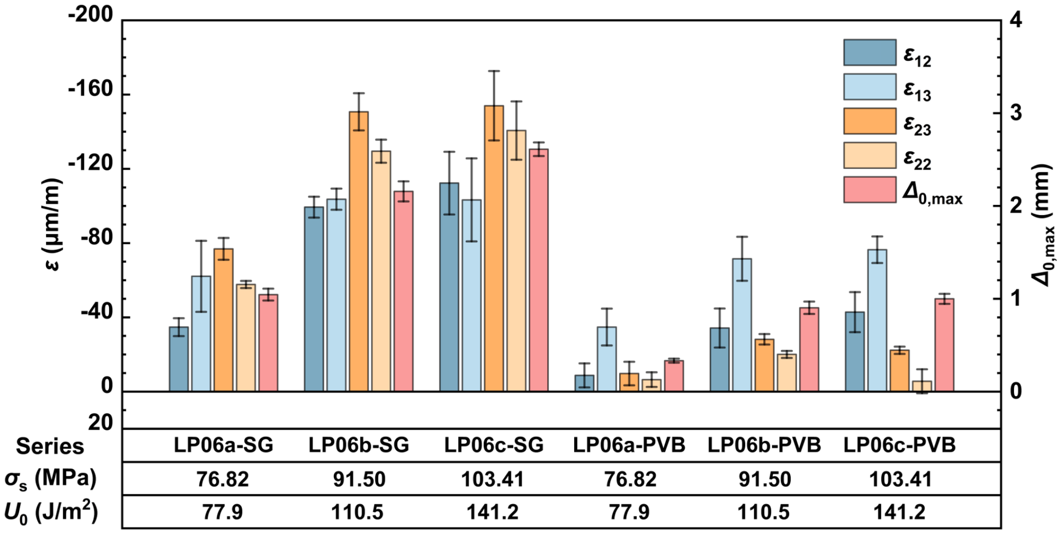

Fig. 19 The comparison of expansion behaviour of the LP06 series

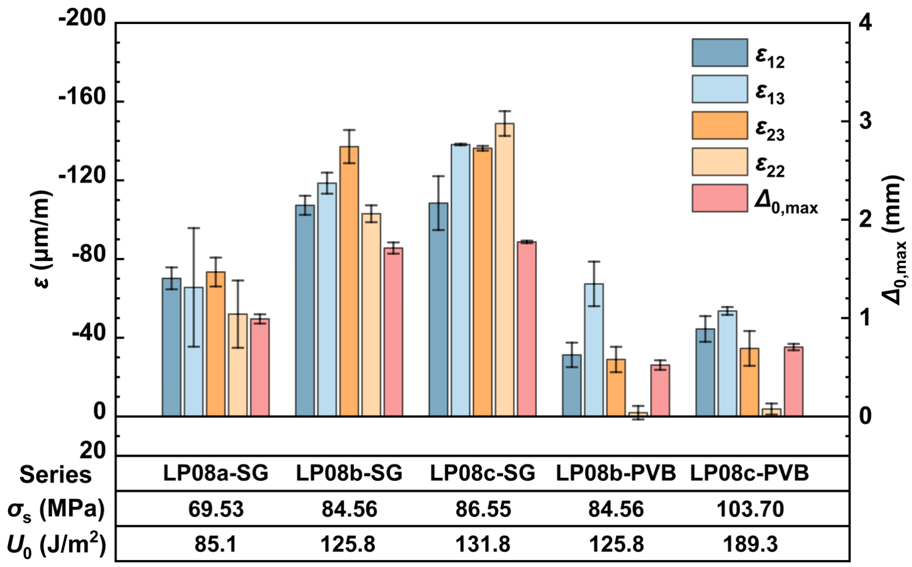

Fig. 20 The comparison of expansion behaviour of the LP08 series

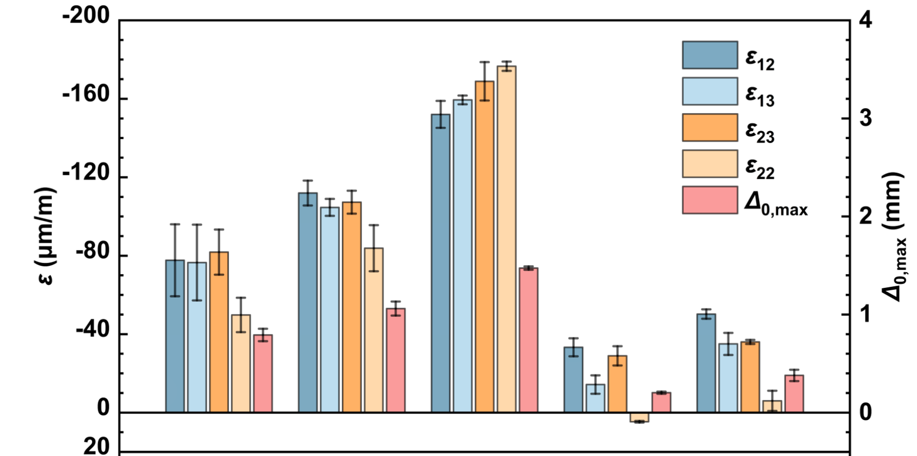

Series	LP12a-SG	LP12b-SG	LP12c-SG	LP12a-PVB	LP12c-PVB
σ_s (MPa)	60.80	71.09	85.23	60.80	94.20
U_0 (J/m^2)	97.6	133.4	191.8	97.6	234.3

Fig. 21 The comparison of expansion behaviour of the LP12 series

3.4.1 Effect of interlayer type

It can be seen from Fig. 19 to Fig. 21 that the interlayer type has a significant impact on both in-plane and out-of-plane expansion of specimens with the same elastic strain energy. Overall, the out-of-plane responses of the SG series are approximately twofold to that of the PVB series. In terms of in-plane responses in the *x*-direction, the responses of SG series are at least 1.5 times than that of the PVB series. This disparity is even more significant in the *y*-direction. For the PVB series, the value of ε_{22} is relatively small, especially for LP08 and LP12 series, and cases like LP12c-PVB (Fig. 21) even show a positive strain. In contrast, all absolute stain values in the *y*-direction for the SG series are above 40 μm/m. When comparing the maximum in-plane response of each specimen, a variation of more than two-fold due to interlayer type difference can be observed.

Fig. 22 provides a more detailed comparison of LP06 series, illustrating the effects of interlayer type on the average expansion responses. The darker lower part of each bar represents the expansion responses of PVB specimens, whilst the lighter upper part indicates the increments of average expansion responses from PVB specimens to SG specimens. The average expansion responses of SG and PVB specimens are displayed above the upper and lower part of each bar, respectively. As can be seen in Fig. 22, differences in in-plane responses between PVB specimens and SG specimens are significant. Particularly noteworthy is the increase in ε_{22} of LP06c series, showing that the strain of SG specimens is 25 times greater than that of PVB specimens. Even in the case of the smallest discrepancy (ε_{13} of LP06c Series), the increasing ratio from PVB specimens to SG specimens still reaches 35.21 %. The observed disparities in in-plane expansion may also be attributed to the higher elastic modulus and adhesive strength of SG compared with PVB. SG interlayer's stiff properties can effectively transfer the fractured glass layer's expansion to the intact glass layer, instead of absorbing the expansion. On the other hand, specimens under asymmetric fracture mode can maintain higher integrity due to the stiffer properties of SG. The SG interlayer can better constrain the in-plane expansion of the fractured glass layer so that the in-plane expansion will be further transformed into the overall out-of-plane deformation of the specimen. Such increments can also be observed in Fig. 22, as the increasing ratios of $\Delta_{0,\,max}$ from PVB specimens to SG specimens are 218 %, 140 % and 161 % for LP06a, LP06b and LP06c, respectively.

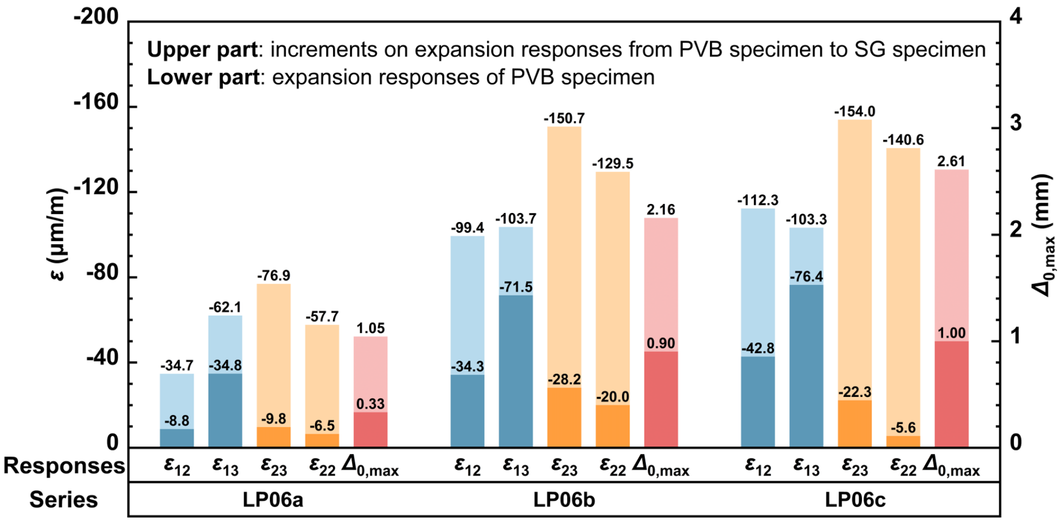

Fig. 22 Effects of interlayer type on the expansion behaviour (LP06 series)

Therefore, it can be inferred that with a higher elastic modulus of interlayer and adhesive strength, the expansion of LG members under asymmetric fracture mode will be greater. Although SG LG members are commonly used as high-performance members in glass structures [58, 59], their greater expansion during the post-fracture stage might increase the risk of further failure, such as buckling due to out-of-plane expansion, compared with PVB LG members.

3.4.2 Effect of elastic strain energy

As explained before, the main drive of the expansion behaviour is the release of stored elastic strain energy at fracture. The fractured glass layer's elastic strain energy per surface area U_0 can indirectly represent the amount of energy introduced to the present LG structure. According to the equivalent temperature differences (ETD) model [30], when each fragment is considered as a cylinder and neglecting the fracture behaviour along the thickness, the fracture strain $\varepsilon_{\mathrm{fr}}$ (with E=70 GPa, v=0.23), which represents the free expansion of a single fragment, can be calculated according to Eq. (7):

$$\varepsilon_{\mathrm{fr}}=\frac{v\text{-}1}{E}\left[a_1\mathrm{sech}\left(\frac{5Ea_2b_1}{t\sigma_{\mathrm{s}}^2(1\text{-}v)}\right)+1\text{-}a_1\right]\sigma_{\mathrm{s}} \tag{7}$$

where t is the thickness of the glass layer, and σ_{s} is the glass layer's surface compressive stress. E and v are the Young's modulus and Poisson ratio of the TTG, respectively. a_1, b_1 and a_2 are constant parameters with values a_1=0.862, b_1=1.686 and a_2=61.05 J/m^2. Through dividing the expansion coefficient α, the equivalent temperature difference can be estimated.

Combining Eq. (2) and Eq. (7), we can obtain the relationship between the fracture strain $\varepsilon_{\mathrm{fr}}$, glass thickness t and elastic strain energy per surface area U_0:

$$\varepsilon_{\mathrm{fr}}=\sqrt{\frac{1\text{-}v}{E}\times\frac{5U_0}{t}}\left[a_1\mathrm{sech}\left(\frac{a_2b_1}{U_0}\right)+1\text{-}a_1\right]\sigma_{\mathrm{s}} \tag{8}$$

The relationship is shown in Fig. 23, covering a glass thickness range from 4 mm to 15 mm and a glass surface compressive stress range from 24 MPa to 120 MPa. The discussed glass surface compressive stress range aims to meet the surface compressive stress provisions on heat-strengthened glass (24-60 MPa) and fully tempered glass (>90 MPa) of Chinese standard GB 15763.2 [33] and GB/T 17841 [60]. It can be seen that all lines show the same increasing trend, i.e., TTG with higher elastic strain energy can yield greater fracture strain. This trend indicates that when the TTG is not restrained, greater free expansion would be observed for a monolithic TTG member with higher elastic strain energy.

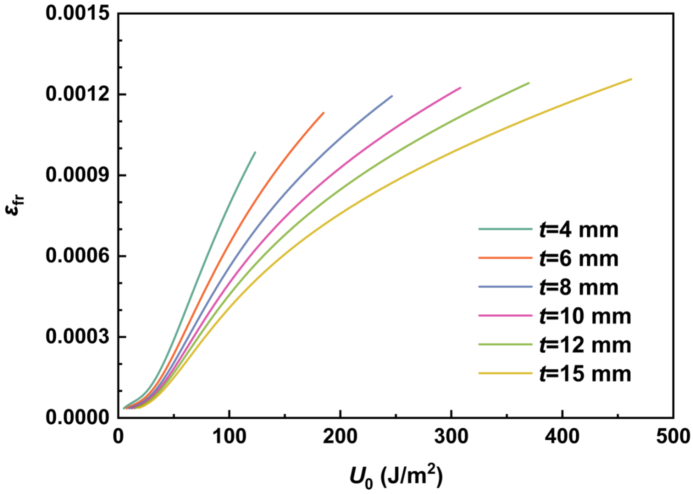

Fig. 23 The relationship between fracture strain ε_{fr}, glass thickness t and elastic strain energy per surface area U_0

However, for current LG plates under asymmetric fracture mode, the free expansion of the fractured glass layer was restrained by both interlayer and intact glass layer. In addition, due to these restraints, the fractured glass layer would have a certain degree of in-plane stiffness, which also plays an important role in resisting the free expansion. Hence, the observed expansion behaviour of LG plates can be described as a state of equilibrium between the free expansion from the fractured glass layer and the counterforce from the interlayer, intact and fractured glass layer. Although the resistance from the interlayer and the intact glass layer could be considered constant in cases with similar interlayer type and glass thickness, the resistance from the fractured glass layer could be influenced by fragment size due to the variations in elastic strain energy. Recent experimental studies on the uniaxial tensile tests of fractured LG specimens [14, 27, 61] indicate that the stiffness of the fractured glass declines with smaller fragment size. However, in the case of expansion analysis at the post-fracture stage, limited research efforts have been dedicated to quantifying the stiffness degradation of fractured glass layer.

It can be concluded that the variations in elastic strain energy of the fractured glass layer have significant effects on the free expansion, as well as the resistance against free expansion. It is important to investigate the resulting expansion behaviours via varying elastic strain energy of the fractured glass layer. The relationship between the fractured glass layer's elastic strain energy per surface area U_0 and average expansion responses is plotted in Fig. 24. To eliminate the stiffness difference of the interlayer and intact glass layer, interlayer type and glass thickness are set to be the same for each subfigure. Although the available number of specimens for each subfigure is limited, the trend of the expansion responses can still be estimated.

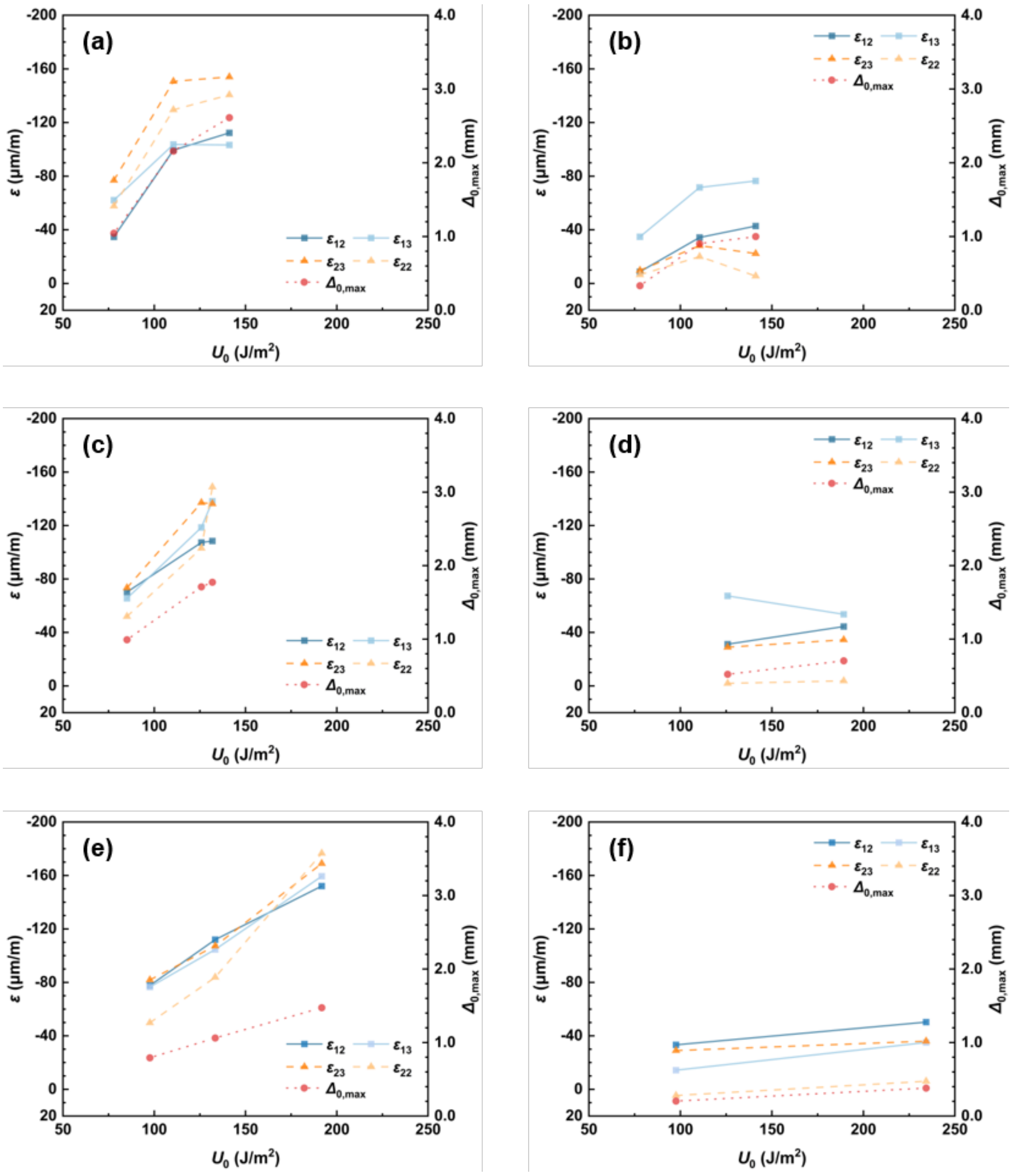

Fig. 24 Effects of elastic strain energy on the expansion behaviour: (a) LP06-SG series; (b) LP06-PVB series; (c) LP08-SG series; (d) LP08-PVB series; (e) LP12-SG series; (f) LP12-PVB series

For the SG series, it can be found that a larger elastic strain energy generally raises all in-plane expansion responses. However, the increasing ratio of expansion responses with elastic strain energy is not constant, it differs according to response types. In Fig. 24(c), as U_0 increases from 85.1 J/m^2 to 125.8 J/m^2, the strain ε_{22} demonstrates the highest rise, reaching a ratio of 98.1 %, whereas the strain ε_{12} shows the lowest rise, with a ratio of approximately half of ε_{22} at 52.9%. A more complex trend can be observed in the effect of U_0 on the expansion responses of PVB series. In the case of LP06-PVB series (Fig. 24(b)), expansion responses such as ε_{12} and ε_{13} grow in a similar manner to LP06-SG series (Fig. 24(a)), while ε_{23} and ε_{22} tend to increase at first and then decrease with rising elastic strain energy. For the LP08-PVB series (Fig. 24(d)) and LP12-PVB series (Fig. 24(f)), augments in U_0 are found to increase the expansion responses, except for ε_{13} in Fig. 24(d). A decrease of 20.4 % is observed in ε_{13} in Fig. 24(d) when U_0 rises from 125.8 J/m^2 to 189.3 J/m^2. It should also be noted that although elastic strain energy increments lead to drops in certain in-plane expansion responses, the maximum in-plane expansion response for both SG series and PVB series generally shows an increasing trend in most cases.

The conclusions regarding the effects of elastic strain energy on out-of-plane expansion responses for both SG and PVB specimens are relatively unified. Similar phenomena can be observed that the increase in U_0 leads to higher out-of-plane deformation $\Delta_{0,\,\max}$. However, the sensitivity of $\Delta_{0,\,\max}$ against elastic strain energy variations U_0 differs. For the 6 mm LG plates, when U_0 increases from 77.9 J/m^2 to 110.5 J/m^2 (an increase of 41.9 %), the increments in $\Delta_{0,\,\max}$ is 1.11 mm for SG series and 0.57 mm for PVB series. For the subsequent elastic strain energy increments (from 110.5 J/m^2 to 141.2 J/m^2, an increase of 27.7 %), the increments for both SG series and PVB series become smaller, with values of 0.45 mm and 0.10 mm, respectively. Although the elastic strain energy values may vary between SG series and PVB series for the cases of LP08 and LP12, it can still be found that specimens with SG interlayer are more sensitive to augments in U_0 compared to those with PVB interlayer in terms of out-of-plane expansion. This can be draw from comparing the slope of the $\Delta_{0,\,\max}$ curves in two corresponding figures, e.g., Fig. 24(c) and Fig. 24(d).

Overall, an increasing elastic strain energy of the fractured glass layer affects both the magnitude of free expansion and the stiffness against free expansion, generally leading to higher in-plane and out-of-plane expansion responses in the present two-layer configuration of LG plates. Significant variations exist in the sensitivity to elastic strain energy variations for specimens with different interlayer types, glass thicknesses and elastic strain energy.

4. Conclusions

The assessment on the post-fracture performance of structural glass members is a critical issue for design, especially for LG members made of thermally tempered glass. The secondary effects due to fragments expansion might increase the fracture or buckling risks of glass members. The present study experimentally investigated the fragment morphology and expansion behaviours of asymmetrically fractured thermally tempered LG plates with different polymeric interlayers and elastic strain energy levels of glass.

A computer-vision-based method was adopted for the image processing of obtained fracture morphology of asymmetrically fractured LG plates. Results show that fragment density has a strong positive linear correlation with elastic strain energy. It is also found that elastic strain energy variations can lead to morphological disparities for LG plates, primarily in terms of fragment shape and uniformity. Two customized energy coefficients were introduced to analyse the fracture surface energy. The findings suggest that fracture surface energy tends to increase with growing elastic strain energy, whilst the transferring rate tends to increase first and then decrease. Detailed comparisons and analyses were then conducted on the two energy coefficients between present LG plates and MG plates. The results indicate that the trends of fragment density and energy coefficients of LG plates with respect to elastic strain energy are consistent with those of MG plates, albeit with variations in values. This is assumed to be attributed to the constraining effects of the intact glass layer and interlayer, as well as the difference in crack initiation locations.

The expansion behaviours, characterized by strain variations on the intact glass and the overall bending deformation, were then examined. It is observed that LG plates will exhibit rapid strain variations on the intact glass layer at fracture, and then stabilize at constant strain values. Moreover, half sinusoid expansion-induced deformation shapes can be observed among the tested LG plates. The effects of interlayer type and elastic strain energy on expansion behaviours were identified by parametric analysis. The results show that SG specimens have more than 2 times greater maximum in-plane and out-of-plane responses compared with corresponding PVB specimens. The stiffer interlayer, SG, can transfer the expansion of fractured glass effectively and instantly, while PVB is more likely to absorb this effect and shows a decayed transfer of expansion. The differences in mechanical properties between PVB and SG interlayers can lead to variations in expansion responses, including the occurrence of secondary cracking and the time required for strain stabilization. Variations in the elastic strain energy of the fractured glass layer not only result in a different free expansion magnitude, but also affect the stiffness against free expansion. Present study indicates that specimens with a higher elastic strain energy generally show greater expansion responses. However, it is also found that specimens with different interlayer type, glass thickness and elastic strain energy have varying degrees of sensitivity towards changes in elastic strain energy. This suggests that, in order to obtain a precise prediction of expansion-induced imperfections, a more in-depth investigation may be required to quantify the expansion behaviour and stiffness degradation at the post-fracture state.

The experimental investigations bridge current data gaps on the expansion behaviours of thermally tempered LG members, especially on the out-of-plane expansion-induced deformation. The presented conclusions provide insights into the post-fracture design of thermally tempered LG members considering their fragments expansion behaviours. This study lays a foundation for expansion prediction through numerical modelling based on fracture morphology reconstruction [12, 43-45]. These models can be further refined by considering factors such as size effect, multi-layered geometries, fracture mode and interlayer thickness.

Data availability

The data that supports the findings of this study are available within the article.

CRediT authorship contribution statement

Yige Wang: Writing – Original Draft, Investigation, Data curation, Visualisation. **Xing-er Wang:** Writing – Review & Editing, Supervision, Funding acquisition. **Jian Yang:** Writing – Review & Editing, Funding acquisition. **Dongdong Xie:** Visualisation. **Kai Pang**: Writing – Review & Editing. **Zhufeng Pan:** Investigation, Data curation.

Declaration of Competing Interest

The authors declare that they have no known competing financial interests or personal relationships that could have appeared to influence the work reported in this paper.

Acknowledgement

This study was funded by the National Natural Science Foundation of China [Grant No. 52078293,51908352].

Appendix

Table A1 Summary of fracture morphology in SG series

Series	Specimen number	Fragment numbers	Fragment density λ_G (10^{-2}·mm^{-2})	Total crack length L_C (mm)	Coefficient φ (10^5·mm^2)	Coefficient ψ (mm/MPa^2)
LP06a-SG	1	1365	0.76	29956	1.797	5.08
	2	1958	1.09	34604	2.076	5.86
	3	1484	0.82	31624	1.897	5.36
LP06b-SG	1	5095	2.83	56890	3.413	6.80
	2	5220	2.90	57902	3.474	6.92
	3	5069	2.82	56873	3.412	6.79
LP06c-SG	1	7810	4.34	68716	4.123	6.43
	2	7154	3.97	66545	3.993	6.22
	3	7775	4.32	68657	4.119	6.42
LP08a-SG	1	1278	0.71	31642	2.531	6.55
	2	939	0.52	25897	2.072	5.36
	3	1186	0.66	30411	2.433	6.29
LP08b-SG	1	3840	2.13	49794	3.984	6.96
	2	3478	1.93	47609	3.809	6.66
	3	3536	1.96	47244	3.780	6.61
LP08c-SG	1	3976	2.21	50176	4.014	6.70
	2	4440	2.47	52624	4.210	7.03
	3	3774	2.10	49647	3.972	6.63
LP12a-SG	1	989	0.55	26440	3.173	7.15
	2	904	0.50	25784	3.094	6.98

	3	792	0.44	26096	3.132	7.06
LP12b-SG	1	1989	1.11	37129	4.455	7.35
	2	1910	1.06	34869	4.184	6.90
	3	1755	0.98	35562	4.267	7.04
LP12c-SG	1	5149	2.86	56139	6.737	7.73
	2	4456	2.48	53373	6.405	7.35
	3	4728	2.63	54307	6.517	7.48

Table A2 Summary of fracture morphology in PVB series

Series	Specimen number	Fragment numbers	Fragment density λ_G (mm^{-2})	Total crack length L_C (mm)	Coefficient φ ($10^5 \cdot mm^2$)	Coefficient ψ (mm/MPa^2)
LP06a-PVB	1	2196	1.22	38765	2.326	6.57
	2	1963	1.09	35919	2.155	6.09
	3	1422	0.79	30927	1.856	5.24
LP06b-PVB	1	5313	2.95	59802	3.588	7.14
	2	4940	2.74	55821	3.349	6.67
	3	5024	2.79	56056	3.363	6.70
LP06c-PVB	1	7334	4.07	68106	4.086	6.37
	2	8328	4.63	72615	4.357	6.79
	3	9856	5.48	77556	4.653	7.25
LP08b-PVB	1	3792	2.11	49665	3.973	6.95
	2	3376	1.88	47314	3.785	6.62
	3	3479	1.93	47859	3.829	6.69
LP08c-PVB	1	6921	3.85	65632	5.251	6.10
	2	7760	4.31	69140	5.531	6.43
	3	6791	3.77	64361	5.149	5.99
LP12a-PVB	1	1059	0.59	26974	3.237	7.30
	2	974	0.54	28806	3.457	7.79
	3	996	0.55	27487	3.298	7.44
LP12c-PVB	1	5121	2.85	57177	6.861	6.44

	2	4949	2.75	57106	6.853	6.44
	3	5160	2.87	56616	6.794	6.38

References

[1] M. Haldimann, A. Luible, M. Overend, Structural use of glass, 1 ed., International Association for Bridge and Structural Engineering, Zurich, 2008.

[2] M. Achintha, A validated modelling technique for incorporating residual stresses in glass structural design, Structures 29 (2021) 446-457.

[3] M. Zaccaria, M. Overend, Nondestructive Safety Evaluation of Thermally Tempered Glass, Journal of Materials in Civil Engineering 32(4) (2020) 04020043.

[4] A. Aronen, R. Karvinen, Effect of glass temperature before cooling and cooling rate on residual stresses in tempering, Glass Structures & Engineering 3(1) (2018) 3-15.

[5] J.H. Nielsen, J.F. Olesen, P.N. Poulsen, H. Stang, Finite element implementation of a glass tempering model in three dimensions, Computers & Structures 88(17) (2010) 963-972.

[6] C. O'Regan, Structural use of glass in buildings, 2 ed., Institution of Structural Engineers, London, 2014.

[7] J.H. Nielsen, J.F. Olesen, H. Stang, Characterization of the Residual Stress State in Commercially Fully Toughened Glass, Journal of Materials in Civil Engineering 22(2) (2010) 179-185.

[8] N. Pourmoghaddam, J. Schneider, Experimental investigation into the fragment size of tempered glass, Glass Structures & Engineering 3(2) (2018) 167-181.

[9] E. Mognato, S. Brocca, Alessandra, Barbieri, Thermally Processed Glass: Correlation Between Surface Compression, Mechanical and Fragmentation Test, Glass Performance Days, Tampere, 2017, pp. 8-11.

[10] H. Lee, S. Cho, K. Yoon, J. Lee, Glass thickness and fragmentation behavior in stressed glasses, New Journal of Glass and Ceramics 2(4) (2012) 116-121.

[11] S. Reich, B. Weller, N. Dietrich, S. Pfefferkorn, Energetic approach of elastic strain energy of thermally tempered glass, Challenging Glass 3: Conference on Architectural and Structural Applications of Glass, Delft, 2012, pp. 509-521.

[12] Y. Zhu, J. Yang, X.-e. Wang, D. Xie, X. Hou, Morphological characterization and reconstruction of fractured heat-treated glass, Journal of Non-Crystalline Solids 616 (2023) 122455.

[13] C. Zhao, J. Yang, X.-e. Wang, I. Azim, Experimental investigation into the post-breakage performance of pre-cracked laminated glass plates, Construction and Building Materials 224 (2019) 996-1006.

[14] Z. Chen, S. Chen, X. Chen, Experimental Study on the Post-fracture Property of Laminated Glass, Proceedings of The 17th East Asian-Pacific Conference on Structural Engineering and Construction, Singapore, 2023, pp. 1316-1326.

[15] N. Pourmoghaddam, M.A. Kraus, J. Schneider, G. Siebert, Relationship between strain energy and fracture pattern morphology of thermally tempered glass for the prediction of the 2D macro-scale fragmentation of glass, Glass Structures & Engineering 4(2) (2019) 257-275.

[16] J.H. Nielsen, Remaining stress-state and strain-energy in tempered glass fragments, Glass Structures & Engineering 2(1) (2017) 45-56.

[17] J.H. Nielsen, M. Bjarrum, Deformations and strain energy in fragments of tempered glass: experimental and numerical investigation, Glass Structures & Engineering 2(2) (2017) 133-146.

[18] A. Kott, T. Vogel, Safety of Laminated Glass Structures after Initial Failure, Structural Engineering International 14(2) (2004) 134-138.

[19] A. Bonati, G. Pisano, G. Royer Carfagni, Redundancy and robustness of brittle laminated plates.

Overlooked aspects in structural glass, Composite Structures 227 (2019) 111288.

[20] D. Xie, J. Yang, C. Zhao, X.-e. Wang, Comprehensive investigation into the thermal rheological behavior and relaxation characteristic of single/composite polymers in laminated glass, Thin-Walled Structures 195 (2024) 111369.

[21] X. Centelles, F. Pelayo, M.J. Lamela-Rey, A.I. Fernández, R. Salgado-Pizarro, J.R. Castro, L.F. Cabeza, Viscoelastic characterization of seven laminated glass interlayer materials from static tests, Construction and Building Materials 279 (2021) 122503.

[22] M. Martín, X. Centelles, A. Solé, C. Barreneche, A.I. Fernández, L.F. Cabeza, Polymeric interlayer materials for laminated glass: A review, Construction and Building Materials 230 (2020) 116897.

[23] F. Pelayo, M.J. Lamela-Rey, M. Muniz-Calvente, M. López-Aenlle, A. Álvarez-Vázquez, A. Fernández-Canteli, Study of the time-temperature-dependent behaviour of PVB: Application to laminated glass elements, Thin-Walled Structures 119 (2017) 324-331.

[24] J. Weis, G. Siebert, Einfluss der Zwischenschicht auf das Bruchverhalten von Verbundsicherheitsglas, ce/papers 5(1) (2022) 241-253.

[25] X.-e. Wang, J. Yang, W.T.A. Chong, P. Qiao, S. Peng, X. Huang, Post-fracture performance of laminated glass panels under consecutive hard body impacts, Composite Structures 254 (2020) 112777.

[26] L. Galuppi, G. Royer-Carfagni, A homogenized analysis à la Hashin for cracked laminates under equi-biaxial stress. Applications to laminated glass, Composites Part B: Engineering 111 (2017) 332-347.

[27] L. Biolzi, M. Orlando, L.R. Piscitelli, P. Spinelli, Static and dynamic response of progressively damaged ionoplast laminated glass beams, Composite Structures 157 (2016) 337-347.

[28] L. Biolzi, S. Cattaneo, M. Orlando, L.R. Piscitelli, P. Spinelli, Post-failure behavior of laminated glass beams using different interlayers, Composite Structures 202 (2018) 578-589.

[29] L. Biolzi, M. Simoncelli, Overall response of 2-ply laminated glass plates under out-of-plane loading, Engineering Structures 256 (2022) 113967.

[30] J.H. Nielsen, J. Schneider, M.A. Kraus, The in-plane expansion of fractured thermally pre-stressed glass panes: -An equivalent temperature difference model for engineering glass design, Construction and Building Materials 327 (2022) 126849.

[31] Y.-g. Wang, X.-e. Wang, J. Yang, Q. Liu, Deformation analysis model of fractured laminated tempered glass considering fragments expansion, Chinese Journal of Applied Mechanics (2024) 1-9 (available online, http://kns.cnki.net/kcms/detail/61.1112.O3.20230506.1011.006.html).

[32] CEN/TS 19100-3, Design of glass structures: Part 3: Design of in-plane loaded glass components and their mechanical joints, Comite Europeen de Normalisation, 2021.

[33] GB 15763.2-2005, Safety glazing materials in building—Part 2:Tempered glass, Standards Press of China, 2005.

[34] L. Kuraray Co., Trosifol® and SentryGlas® Architectural Glazing for Laminators. https://www.trosifol.com/fileadmin/user_upload/tools/downloads/product-brochures/architectural_glazing_laminators/Trosifol_SentryGlas_Architectural-Glazing_for_laminators.pdf, 2024 (accessed 24 June 2024).

[35] J. Belis, D. Mocibob, A. Luible, M. Vandebroek, On the size and shape of initial out-of-plane curvatures in structural glass components, Construction and Building Materials 25(5) (2011) 2700-2712.

[36] L. Valarinho, J.R. Correia, M. Machado-e-Costa, F.A. Branco, N. Silvestre, Lateral-torsional

buckling behaviour of long-span laminated glass beams: Analytical, experimental and numerical study, Materials & Design 102 (2016) 264-275.
[37] Q. Yu, K. Zhang, C. Cui, R. Zhou, F. Cheng, R. Ye, Y. Zhang, Method of thickness measurement for transparent specimens with chromatic confocal microscopy, Appl. Opt. 57(33) (2018) 9722-9728.
[38] A. Miks, J. Novak, P. Novak, Analysis of method for measuring thickness of plane-parallel plates and lenses using chromatic confocal sensor, Appl. Opt. 49(17) (2010) 3259-3264.
[39] EN 12150-1, Glass in building - Thermally toughened soda lime silicate safety glass - Part 1: Definition and description, Comite Europeen de Normalisation, 2015.
[40] J. Schindelin, I. Arganda-Carreras, E. Frise, V. Kaynig, M. Longair, T. Pietzsch, S. Preibisch, C. Rueden, S. Saalfeld, B. Schmid, J.-Y. Tinevez, D.J. White, V. Hartenstein, K. Eliceiri, P. Tomancak, A. Cardona, Fiji: an open-source platform for biological-image analysis, Nature Methods 9(7) (2012) 676-682.
[41] I. Arganda-Carreras, V. Kaynig, C. Rueden, K.W. Eliceiri, J. Schindelin, A. Cardona, H. Sebastian Seung, Trainable Weka Segmentation: a machine learning tool for microscopy pixel classification, Bioinformatics 33(15) (2017) 2424-2426.
[42] D. Legland, I. Arganda-Carreras, P. Andrey, MorphoLibJ: integrated library and plugins for mathematical morphology with ImageJ, Bioinformatics 32(22) (2016) 3532-3534.
[43] N. Pourmoghaddam, M.A. Kraus, J. Schneider, G. Siebert, The geometrical properties of random 2D Voronoi tesselations for the prediction of the tempered glass fracture pattern, ce/papers 2(5-6) (2018) 325-339.
[44] X.-e. Wang, J. Yang, X. Huang, F. Wang, Y. Zhu, Voronoi-FDEM concept for modelling post-fracture response of progressively damaged structural glass, Engineering with Computers 38(4) (2022) 3025-3038.
[45] X.-e. Wang, J. Yang, Z. Pan, F. Wang, Y. Meng, Y. Zhu, Exploratory investigation into the post-fracture model of laminated tempered glass using combined Voronoi-FDEM approach, International Journal of Mechanical Sciences 190 (2021) 105989.
[46] R. Dugnani, R.J. Zednik, P. Verghese, Analytical model of dynamic crack evolution in tempered and strengthened glass plates, International Journal of Fracture 190(1) (2014) 75-86.
[47] N. Pourmoghaddam, On the fracture behaviour and the fracture pattern morphology of tempered soda-lime glass, 1 ed., Springer Vieweg Wiesbaden, Frankfurt am Main, 2019.
[48] C.L. Okafor, D.M. Martin, The Effect of Temperature on the Fracture-Surface Energy of A Waste Disposal Glass, Journal of the American Ceramic Society 65(2) (1982) 87-90.
[49] S.M. Wiederhorn, Fracture Surface Energy of Glass, Journal of the American Ceramic Society 52(2) (1969) 99-105.
[50] X. Zhang, H. Liu, C. Maharaj, M. Zheng, I. Mohagheghian, G. Zhang, Y. Yan, J.P. Dear, Impact response of laminated glass with varying interlayer materials, International Journal of Impact Engineering 139 (2020) 103505.
[51] X. Centelles, M. Martín, A. Solé, J.R. Castro, L.F. Cabeza, Tensile test on interlayer materials for laminated glass under diverse ageing conditions and strain rates, Construction and Building Materials 243 (2020) 118230.
[52] Y. Lu, S. Chen, X. Shao, Shear modulus of ionomer interlayer: Effects of time, temperature and strain rate, Construction and Building Materials 302 (2021) 124224.
[53] P.A. Hooper, B.R.K. Blackman, J.P. Dear, The mechanical behaviour of poly(vinyl butyral) at different strain magnitudes and strain rates, Journal of Materials Science 47(8) (2012) 3564-3576.

[54] T. Sakai, M. Ramulu, A. Ghosh, R.C. Bradt, Cascadating fracture in a laminated tempered safety glass panel, International Journal of Fracture 48(1) (1991) 49-69.

[55] K. Takahashi, Fast fracture in tempered glass, Key Engineering Materials 166 (1999) 9-18.

[56] S. Aratani, Y. Yamauchi, K. Oginoh, K. Takahashi, Generation of Secondary Cracks in Tempered Soda-Lime-Silica Glass, Journal of the Ceramic Society of Japan 101(4) (1993) 506-507.

[57] Z. Tang, M.B. Abrams, J.C. Mauro, L.R. Zoeller, N. Venkataraman, G. Hu, High-speed camera study of Stage III crack propagation in chemically strengthened glass, Applied Physics A 116(2) (2014) 471-477.

[58] L. Riddell-Smith, L. Cunningham, P. Mandal, Experimental study of 3-ply laminated glass beams subject to in-plane loads, Structures 33 (2021) 3984-3998.

[59] X. Centelles, J.R. Castro, F. Pelayo, M. Aenlle-López, L.F. Cabeza, Experimental study and comparison of different fully transparent laminated glass beam designs, Glass Structures & Engineering 6(4) (2021) 463-486.

[60] GB/T 17841-2008, Heat strengthened glass, Standards Press of China, 2008.

[61] M. Botz, M.A. Kraus, G. Siebert, Untersuchungen zur thermomechanischen Modellierung der Resttragfähigkeit von Verbundglas, ce/papers 3(1) (2019) 125-136.